

Title	超薄Mo1-XNbxS2層の作製と熱電物性の研究
Author(s)	Pham, Thi Xuan
Citation	
Issue Date	2018-12
Type	Thesis or Dissertation
Text version	ETD
URL	http://hdl.handle.net/10119/15761
Rights	
Description	Supervisor:小矢野 幹夫, マテリアルサイエンス研究科, 博士

Doctoral Dissertation

Fabrication and Thermoelectric Properties
of Ultrathin Layer of $\text{Mo}_{1-x}\text{Nb}_x\text{S}_2$

Pham Xuan Thi

Supervisor: Prof. Mikio Koyano

School of Materials Science

Japan Advanced Institute of Science and Technology

December 2018

Fabrication and Thermoelectric Properties of Ultrathin Layer of $\text{Mo}_{1-x}\text{Nb}_x\text{S}_2$

Pham Xuan Thi

A Dissertation Submitted to
the School of Materials Science
Japan Advanced Institute of Science and Technology
in partial fulfillment of the requirements
for the degree of Doctor of Philosophy

December 2018

Approved by
Prof. Mikio Koyano

This certifies that the Ph. D. Dissertation
of Pham Xuan Thi is approved.

Thesis Committee Head: Prof. Mikio Koyano

Thesis Committee Member: Prof. Hiroshi Mizuta

Thesis Committee Member: Prof. Junichiro Shiomi

Thesis Committee Member: Associate. Prof. Dam Hieu Chi

Thesis Committee Member: Associate. Prof. Masashi Akabori

Thesis Supervisor: Prof. Mikio Koyano

School of Materials Science

Japan Advanced Institute of Science and Technology

December 2018

Abstract

Recent remarkable advances in two-dimensional (2D) materials have spurred studies examining thermoelectric (TE) applications, especially thin and flexible TE transducers. Among them, 2D MoS₂ has become the candidate for TE materials because it has not only high power factor but also unique properties for TE devices, such as high mechanical flexibility and in-plane mechanical stiffness. The large power factor of n-type MoS₂ ultrathin layers has been obtained by using the field effect transistor (FET) structure. However, the usage of an external back-gate to modulate the carrier concentration in pristine MoS₂ produces a complicated technique for device fabrication and creates difficulty for practical application for thermoelectrics. Moreover, the TE properties of the p-type doped MoS₂ ultrathin layers, which are fundamentally necessary for TE devices that consist of n-type and p-type TE elements, have not been studied even though the p-type Nb-doped MoS₂ have been synthesized in which Mo is substituted by Nb.

In this research, I aim to investigate the TE properties of p-type Nb-doped MoS₂ ultrathin layers. The effects of Nb on TE transport properties will be assessed in relation to the behavior of electrical resistivity and the Seebeck coefficient depending on the temperature, and first principles calculations of the density of states (DOS).

To carry out the research, I first synthesized the single crystals by using the chemical vapor transport method. Then I designed and fabricated the devices of these ultrathin layers that were mechanically exfoliated from my synthesized crystals. The reliability of fabricated devices was supported by the evaluation of the contact resistance and the simulation of the temperature profile by using finite element-method software Flow 3D. Finally, electrical resistivity and the Seebeck coefficient measured in the temperature range from 300 K to 450 K are analyzed and compared with first principles calculations of the DOS.

The experimentally obtained results and density functional theory calculations indicate the

p-type degenerate semiconducting behavior of ultrathin layers. The enhancement of electrical resistivity compared to the bulk Nb-doped MoS₂ results from weak localization and carrier scattering of the conduction carriers by random potential originated from stacking faults or/and edge roughness. This picture is consistent with the decrease in electrical resistivity with rising temperature. Moreover, the lack of change of the Seebeck coefficient by layer thickness suggests that the modulation of spectral conductivity $\Sigma(E, T)$ is cancelled even in the localization condition. The experimental results are also consistent with first principles calculations for the density of states of pristine MoS₂ and Nb-doped MoS₂ monolayers.

By analyzing the physical mechanism of the influence of the Nb dopants on TE transport properties of Nb-doped MoS₂ ultrathin layer, this research contributes partly to the field of 2D TE materials. This research also offers a potential trend for next-generation flexible 2D TE materials which are applied in TE nanodevices.

KEYWORDS: MoS₂, thermoelectric properties, ultrathin layer, weak localization, first-principles calculations.

Table of Contents

Abstract	i
Table of Contents	ii
Chapter 1	1
Introduction	1
1.1 Thermoelectric materials.....	1
1.2 History of methodology for improving <i>ZT</i>	4
1.3 Current researches on two dimensional TE materials	6
1.4 Research objective and dissertation outline	10
Chapter 2	12
Synthesis of Mo_{1-x}Nb_xS₂ single crystals	12
2.1 Introduction	12
2.2 Synthesis of Mo _{1-x} Nb _x S ₂ single crystals.....	12
2.2.1 Preparation of clean quartz ampoules	12
2.2.2 Introduction of the powdered materials and transport agent into quartz tubes...	13
2.2.3 Sealing off the ampoules	14
2.2.4 Synthesis	15
2.3 Results and discussion.....	16
2.4 Micromechanical exfoliation and atomic force microscope	19
2.5 Conclusion.....	20
Chapter 3	22
Device fabrication of ultrathin layers of Nb-doped MoS₂	22
3.1 Introduction	22
3.2 Design of device fabrication of ultrathin layers	22
3.3 Fabrication the patterns of markers	23
3.3.1 Preparation of clean substrates.....	23
3.3.2 Spin coating and electron beam lithography.....	24
3.3.3 Deposition and lift-off.....	25
3.4 Fabrication of electrodes for transferring ultrathin layers.....	26
3.5 Mechanical exfoliation of ultrathin layers and transferring	27
3.5.1 Checking the electrical status of electrodes	27
3.5.2 Preparation of ultrathin layers and transferring	29
3.6 Device fabrication for measurement of the temperature dependence of <i>S</i> of the heavily	

doped n-type silicon wafer.....	32
3.7 Simulation of the temperature profile	33
3.8 Conclusion.....	38
Chapter 4.....	39
Results and Discussion	39
4.1 Introduction	39
4.2 Measurement of S of heavily doped n-type Si	39
4.3 Measurement of ρ and S of ultrathin layers	40
4.3.1 Measurement of ρ	41
4.3.2 Measurement of S	45
4.4 Discussion	51
4.5 Conclusion.....	59
Chapter 5.....	60
Conclusions and Future Work	60
Bibliography	63
Acknowledgements.....	72
List of Figures	73
List of Tables	77
List of activities.....	78

Chapter 1

Introduction

1.1 Thermoelectric materials

Thermoelectric (TE) technology, which is based on Seebeck effect and Peltier effect [1], directly converts waste heat into electrical energy and vice versa, by utilizing power generators and Peltier coolers, respectively. This environmentally friendly technology has been attracting a lot of attention for decades because of the fact that, more than 60% of energy, mostly in the form of waste heat, as illustrated in figure 1.1 [2], is lost in useless worldwide. Although these TE devices present many benefits such as solid-state operation, high reliability, and good stability [1, 3, 4], they remain limited to niche application because of their low power conversion efficiency [5, 6]. For instance, the TE heat pumps are used in the back and bottom cushions (figure 1.2) [6], in which the conditioned air moves from the TE system through channels to the occupant, supplying on-demand cooling or heating.

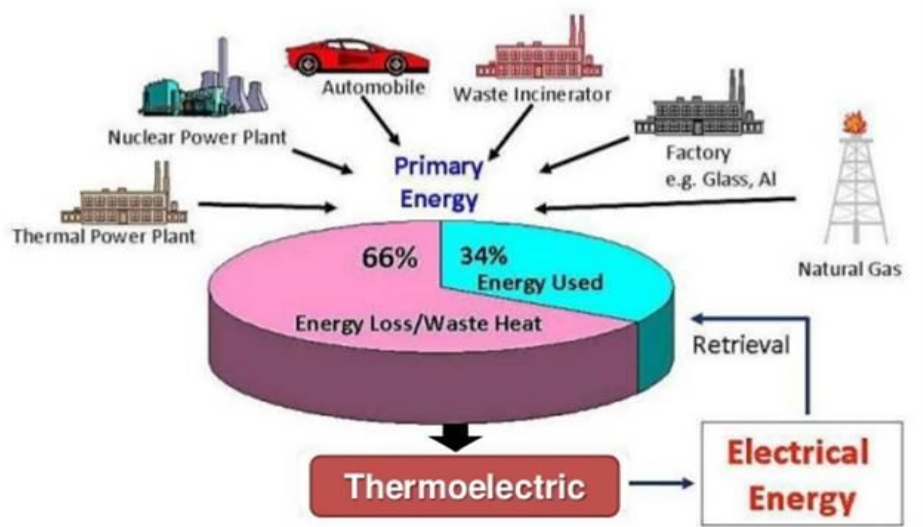


Figure 1.1 Energy Statistics and potential TE Generators [2].

The low power conversion efficiency of TE devices is related directly to the low conversion efficiency of the TE materials, which can be evaluated by power factor $PF = S^2 \rho^{-1}$

and the dimensionless figure of merit as below

$$ZT = (S^2T)/(\rho\kappa) \quad (1-1)$$

where S is the Seebeck coefficient, ρ represents electrical resistivity, κ denotes thermal conductivity, and T is temperature [7]. The quantity PF is the key to achieving high ZT . Large PF is equivalent to large generation of the voltage and current. Thermal conductivity $\kappa = \kappa_l + \kappa_e$ consists of the contribution from lattice vibrations κ_l , called lattice thermal conductivity, and from carrier κ_e , called carrier thermal conductivity. In fact, the intrinsically compromised behavior between S , ρ and κ causes a challenging issue for the enhancement of efficiency [8]. For example, large S concomitantly results in large ρ and low κ . Typically, good TE materials belong to degenerate semiconductors [9, 10] that have the carrier concentrations within the region of 10^{19} – 10^{21} cm^{-3} , as shown in figure 1.3 [9].

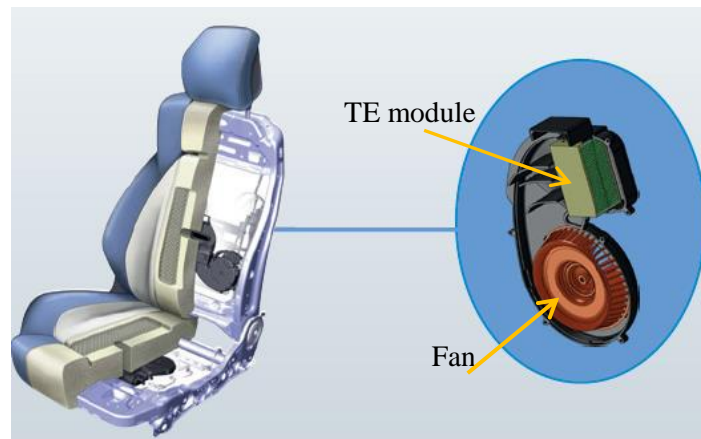


Figure 1.2 Automotive Climate Control Seat developed by Gentherm [6].

Thermoelectricity was discovered since the birth of the Seebeck effect in 1821 by the German scientist T. J. Seebeck (figure 1.4(a)) [11, 12]. When a temperature difference ΔT is applied to a TE couple consisting of n-type (electrons are majority carriers) and p-type (holes are majority carriers) elements, the mobile charge carriers will diffuse from the hot side to the cold side, generating an electrostatic potential ΔV . The ratio of $-\Delta V/\Delta T$ is related to an intrinsic property of the materials called the Seebeck coefficient S , or thermopower, as shown

in figure 1.4(b). Conversely, when a current is applied to a TE couple, heat is absorbed in one junction and released at the other. This effect was discovered in 1834 by French physicist J. C. A. Peltier (figure 1.4(d)) known as the Peltier effect, as displayed in figure 1.4(e) [13].

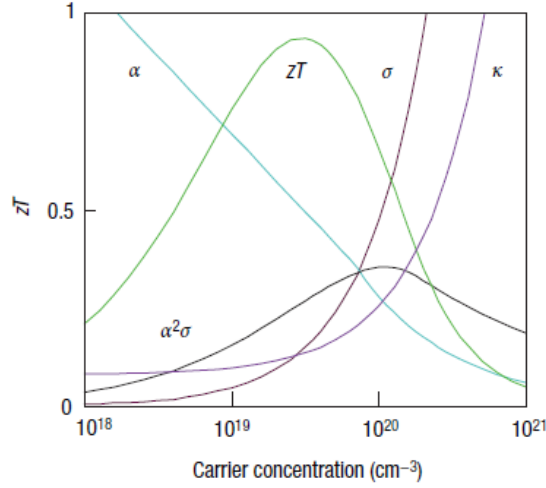


Figure 1.3 Good TE materials are typically heavily doped semiconductors (carrier concentration between 10^{19} and 10^{21} carriers per cm^3) [9].

For power generation using the Seebeck effect, the TE efficiency η_p is determined by the relationship between Carnot efficiency ($(T_h - T_c)/T_h$) and ZT as following equation [14, 15],

$$\eta_p = \frac{T_h - T_c}{T_h} \left[\frac{\sqrt{1 + ZT_{\text{ave}}} - 1}{\sqrt{1 + ZT_{\text{ave}}} + T_c/T_h} \right] \quad (1-2)$$

where ZT_{ave} is the average value per leg (n-type and p-type legs) and is averaged over the ZT curve depending on temperature between T_h and T_c , that are the hot and cold sides of the temperature in sequence.

$$ZT_{\text{ave}} = \frac{1}{T_h - T_c} \int_{T_c}^{T_h} ZT dT \quad (1-3)$$

Figure 1.4(c) shows that the conversion efficiency becomes larger at higher ZT_{ave} and larger temperature difference.

For refrigeration based on the Peltier effect, the TE cooling efficiency η_c can be evaluated by equation (1-4) [14, 15],

$$\eta_c = \frac{T_h}{T_h - T_c} \left[\frac{\sqrt{1 + ZT_{\text{ave}}} - T_h/T_c}{\sqrt{1 + ZT_{\text{ave}}} + 1} \right] \quad (1-4)$$

As illustrated in Fig 1.4(f), similar to the TE power generation, a larger ZT_{ave} value will produce a higher TE cooling efficiency η_c .

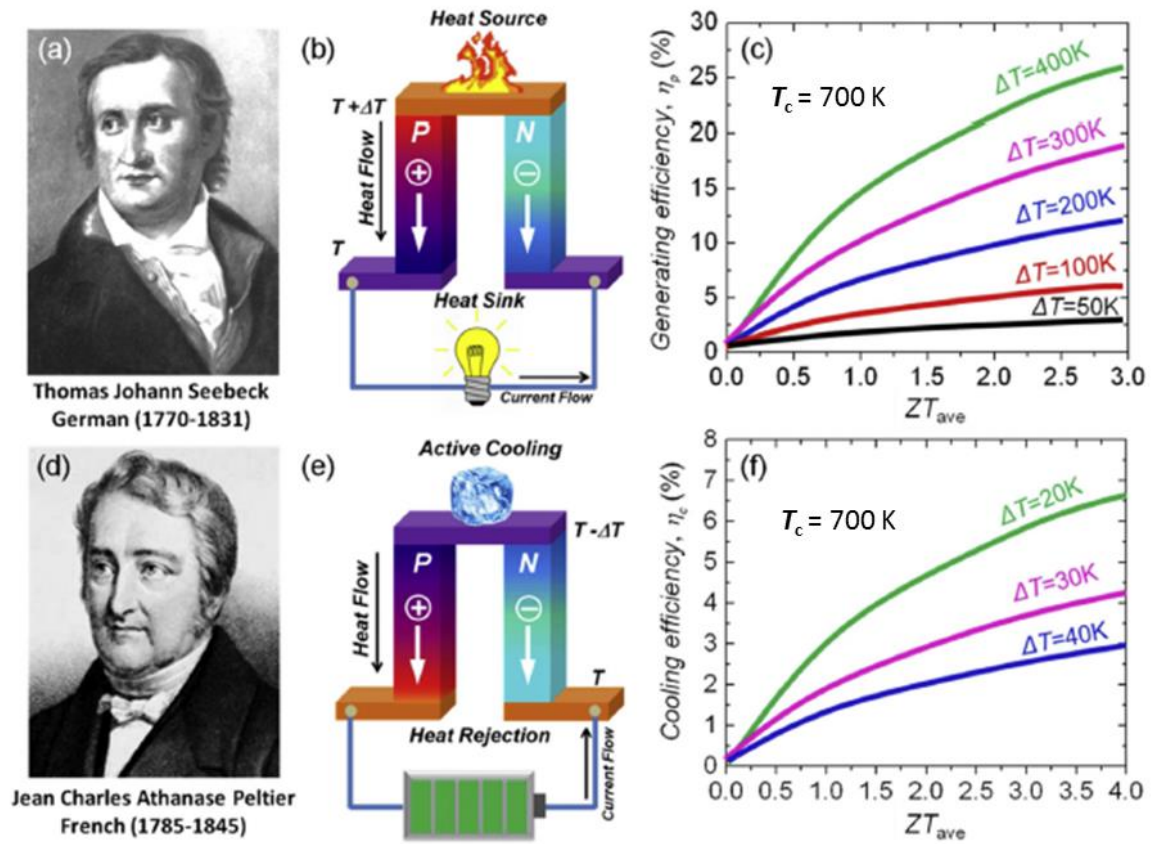


Figure 1.4 The Seebeck and Peltier effects: (a) The German physicist, T. J. Seebeck, (b) power generation produced by applying a temperature difference to make charge carriers to diffuse from the hot end to the cold end, (c) power generation efficiency in relation to ZT_{ave} ; (d) the French physicist, J. C. A. Peltier, (e) active refrigeration produced by absorbing heat at the lower junction and releasing heat at the higher junction when applying a current through the circuit, (f) cooling efficiency in relation to ZT_{ave} . High ZT_{ave} corresponds to high TE power generation and cooling efficiency [11].

1.2 History of methodology for improving ZT

As mentioned above, the desire for producing TE materials having high ZT have faced with big challenges because power factor PF and thermal conductivity κ determined by the electronic structure and scattering of charge carriers (electrons or holes) are not independently controllable [8, 11]. In the 1950s, the attempts eventually confirmed that the alloyed

semiconductors with high carrier concentration are the most efficient bulk TE materials. Many experiments showed that Bi_2Te_3 and alloys like $\text{Bi}_x\text{Sb}_{2-x}\text{Te}_3$, and PbTe and alloys like PbTe-PbSe display high ZT up to 1 [16, 17]. The reason is that these alloyed semiconductors suppress the transport of phonons (quantized lattice vibrations carrying heat), resulting in a reduction of κ meanwhile maintaining high carrier concentration for good electrical conductivity σ . In addition, the usage of heavy elements with low sound velocities, such as Bi, Te, and Pb, results in the further reduction of κ_1 [8]. However, the increase in σ by rising carrier concentrations also depresses S and enhances $\kappa_e = L\sigma T$ proposed by Wiedemann–Franz, where L stands for the Lorenz number. Therefore, the choice for reduction of the electronic component of κ of TE materials is impossible because it will negatively influence on σ leading to no improvement to ZT . These compromised trends are illustrated in figure 1.3 and prevent the ability to improve ZT . That why over the following three decades, from 1960 to 1990, there was no significant progress in improving ZT , and the $(\text{Bi}_{1-x}\text{Sb}_x)_2(\text{Se}_{1-y}\text{Te}_y)_3$ alloy family remained the best material with maximal value $ZT \approx 1$ [17].

In the 1990s, TE community was motivated by the advances in TE materials with the novel discoveries for improving the TE performance. There have been two different approaches for the next generation of TE materials by utilizing new groups of bulk TE materials with complicated crystal structures and low-dimensional TE materials. The first approach called the “phonon glass electron crystal” (PGEC) approach [18] supposes that the best TE materials should combine the thermal properties of glass-like materials and electrical properties of crystal-like materials. This approach is successful for materials having complex crystal structures, in which the voids caused by vacancies and rattlers caused by heavy element atoms located in the voids could display as effective phonon scattering centers and result in the significant reduction of κ_1 [19]. The second approach is based on the idea of Hicks and Dresselhaus [20-23], who proposed that low-dimensional TE materials could

increase ZT via the enhancement of S due to quantum confinement, and/or the decrease of κ_L due to the increase of surface scattering. Firstly, because of size-quantization effects, S in low-dimensional systems becomes significantly larger than that of 3D systems. According to the Mott relation, in systems with degenerate Fermi statistics, such as degenerate semiconductors and metals, S is given by [24]

$$S = \frac{\pi^2 k_B}{3q} k_B T \left\{ \frac{d[\ln(\sigma(E))]}{dE} \right\} \Big|_{E=E_F} \quad (1-5)$$

where, $\sigma(E)$ is electrical conductivity and satisfies,

$$\sigma(E) = qn(E)\mu(E) \quad (1-6)$$

where, $n(E)$ denotes the carrier concentration, $\mu(E)$ is the mobility. It is clear from equation (1-5) that, the enhancement of the energy-dependence of electrical conductivity $d\sigma(E)/dE$ will increase S . From equation (1-6), the enhancement of $d\sigma(E)/dE$ is equivalent to the enhancement of $dn(E)/dE$ and/or $d\mu(E)/dE$. The increase in $dn(E)/dE$ can be gained by improving the dependence of density of states (DOS) on energy. As shown in figure 1.5, the size-quantization effect in low-dimensional structures leads to the increase in $dn(E)/dE$. Secondly, low-dimensional systems lead to the reduction of κ_L without too much loosing on mobility μ because the phonon mode structure is influenced by the low dimensionality, or the electron mean free path is less than the phonon mean free path.

1.3 Current researches on two dimensional TE materials

The idea of Hicks and Dresselhaus combining with the recent remarkable advances in two-dimensional (2D) materials [25], after the birth of graphene, has enticed researchers to be interested in TE application of 2D materials, for example, planar Peltier cooling [26]. With many unique properties that are best suitable for electronic and optoelectronic applications, transition metal dichalcogenides [27, 28] are attracting much attention. Among them, 2D molybdenum disulfide (MoS_2) is the candidate for TE investigation due to its unique

properties for electronic devices [29-32], such as large band gap [33] high mechanical flexibility [34] and in-plane mechanical stiffness [35].

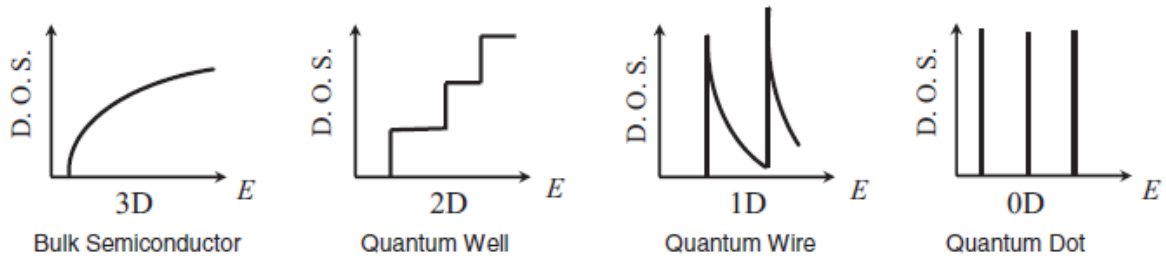


Figure 1.5 Electronic DOS for (a) 3D crystalline semiconductor, (b) 2D quantum well, (c) 1D nanowire or nanotube, and (d) 0D quantum dot [23].

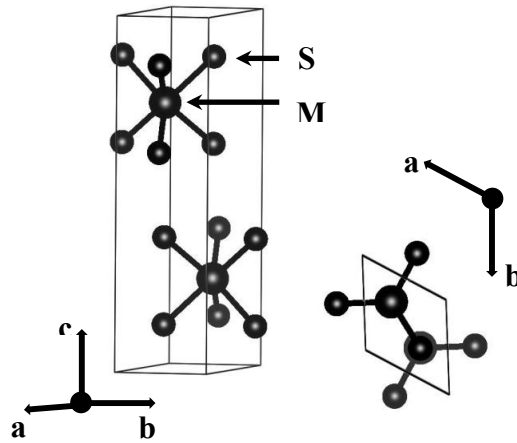


Figure 1.6 Supercell and crystal structure of bulk MoS₂.

Structurally, the Nb-doped MoS₂ single crystal is similar to pristine MoS₂. Bulk MoS₂ is a semiconductor with a band gap of 1.2 eV [36]. It has the layered structure consisting of a stack of individual layers in which each layer composed of a single atomic triangular plane of molybdenum (Mo) is sandwiched between two triangular planes of sulfur (S), all bonded by strong covalent bonding (figure 1.6) [37]. The individual layers of 0.65 nm, held together by weak van der Waals forces [38], enable us to extract the ultrathin layers using micromechanical exfoliation [39].

TE properties of 2D MoS₂ have been studied by both experimentally [40, 41] and theoretically [42, 43]. Experimentally, using scanning photocurrent spectroscopy of MoS₂

transistors, Buscema *et al.* demonstrated that the Seebeck coefficient S of single-layer MoS₂ can be up to be $-10^5 \mu\text{V/K}$ [40], in which the carrier concentration can be tuned by an external electric field. Similarly, Jing Wu *et al.* [41] recently obtained the large S about -30 mV/K in MoS₂ monolayer in insulating regime applied by a negative back gate voltage (figure 1.7). Compared to value of S of other recently studied low-dimensional materials, such as graphene ($\pm 100 \mu\text{V/K}$) [44], Bi₂Te₃ ($\pm 200 \mu\text{V/K}$) [45, 46] semiconducting carbon nanotubes ($-300 \mu\text{V/K}$) [47], Ge–Si core–shell nanowires ($400 \mu\text{V/K}$) [48] and InAs nanowires (-5 mV/K) [49], this value is remarkably larger. However, ZT value of MoS₂, in this case, is predicted rather low due to large electrical resistivity ρ [41].

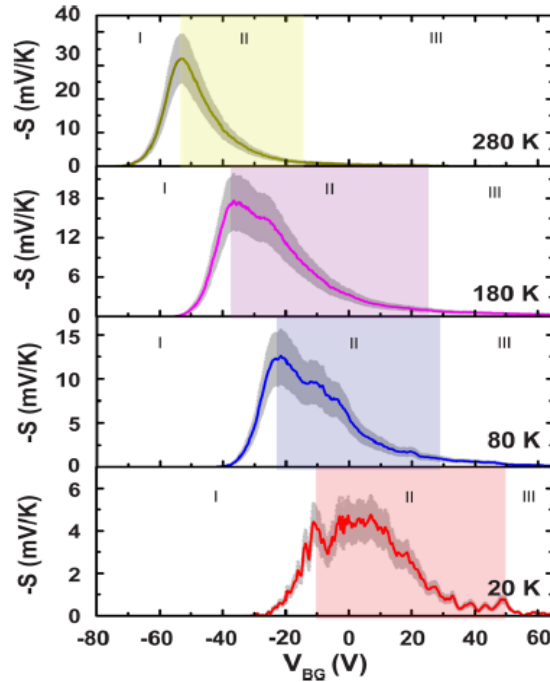


Figure 1.7 Large Seebeck coefficient of single layer MoS₂ as a function of back gate voltage at different temperatures [41].

Recently, Kayyalha *et al.* carried out a systematic investigation of the thickness dependence of the electrical and TE properties of the MoS₂ ultrathin layers [50]. They discovered that by increasing the positive back-gate voltage to shift the Fermi level (E_F) of sample to enhance the carrier concentration, a large power factor PF about $30 \mu\text{Wcm}^{-1} \text{K}^{-2}$ in

the bilayer was obtained as illustrated in figure 1.8. This result was also confirmed by K. Hippalgaonkar *et al.* [51] when obtaining the large power factor of monolayer, bilayer, and trilayer of MoS₂ when investigating the metallic regime by applying a positive back gate. Even though the magnitude of S decreases when the Fermi level is shifted closer to the conduction band minimum (CBM) due to the enhancement of electron concentration, the increase in electrical conductivity leads to improvement of the measured power factor $S^2\sigma$. This ultrathin layer n-type MoS₂ with high power factors are promising TE applications. However, the usage of external back-gate to modulate the carrier concentration in pristine MoS₂ results in complicated technique for device fabrication and difficulty for practical application.

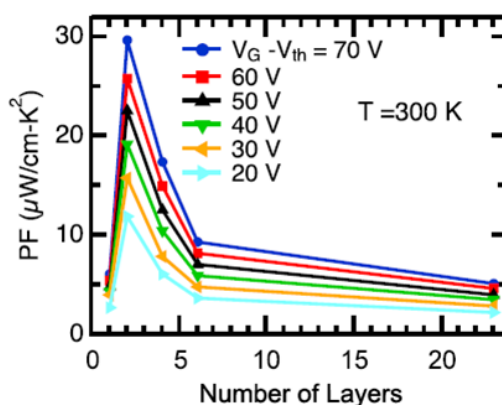


Figure 1.8 Power factor of thin layer MoS₂ as a function of the V_G [50].

Another method published recently is the substitution, in which molybdenum (Mo) is replaced by niobium (Nb). Until now, stable p-type single crystals of MoS₂ by substitutional Nb doping were synthesized by using chemical vapour transport (CVT) method [52, 53]. This is proved by using density-functional energetics/formation energies calculations that Nb (4d⁴5s¹) which has one less valence electron than Mo (4d⁵5s¹) is theoretically proposed as the most suitable substitutional acceptor [54]. Using CVT method, J. Suh *et al.* [52] synthesized the stable p-type conduction in MoS₂ by substitutional 0.5% Nb doping resulting in a degenerate hole density of $\sim 3 \times 10^{19} \text{ cm}^{-3}$ that belong to the optimal region for achieving the

high efficiency of TE material. In contrast to n-type behavior in FET of pristine MoS₂, the Nb-doped MoS₂ ultrathin layers have been theoretically and experimentally demonstrated to be the degenerate p-type semiconductors [52-55], which are critical needs for TE devices which consist of n-type and p-type TE elements [9]. To my knowledge, no report of the relevant literature has described p-type TE ultrathin layers. Moreover, the effects of the Nb dopants on the TE properties of Nb-doped MoS₂ ultrathin layers have not been considered.

1.4 Research objective and dissertation outline

The objective of this dissertation is the fabrication of the devices of the p-type degenerate ultrathin layers of Nb-doped MoS₂ and the measurement of their TE properties. To achieve this goal, I first synthesize the crystallinity of single crystals of Mo_{0.97}Nb_{0.03}S₂ by using CVT method. Then I apply the micromechanical exfoliation to extract the ultrathin layers from synthesized bulk materials. Next, the devices of ultrathin layers are fabricated based on the design. After that, electrical resistivity ρ and the Seebeck coefficient S over the temperature range from 300 K to 450 K are measured. Finally, the experimental results are compared with that of density functional theory (DFT) calculations for DOS of pristine MoS₂ and Nb-doped MoS₂ monolayer.

In this research, my purpose is to investigate the TE properties of Nb-doped MoS₂ ultrathin layers and the effects of the Nb dopants on their TE transport properties in relation to the behavior of S , ρ , and DOS. This dissertation consists of five chapters described as follows.

In chapter 1, the general introduction of the research is introduced together with the organization of the thesis. The process for synthesizing the single crystals of MoS₂, Mo_{0.99}Nb_{0.01}S₂, Mo_{0.98}Nb_{0.02}S₂, and Mo_{0.97}Nb_{0.03}S₂ is presented in detail in chapter 2. This chapter also describes the analysis of X-ray powder diffraction (XRD) for getting the lattice parameters. The XRD patterns and the mechanical exfoliation technique suggest the success of the synthesis of single crystals by using CVT method. The fabrication of the devices is

presented step by step in chapter 3. It consists of the preparation of the suitable substrate, pre-markers, electron beam lithography (EBL), thermal deposition, transferring system, and annealing. Furthermore, the device of the Si substrate is fabricated for determining its Seebeck coefficient. The reliability of the fabricated devices is also testified by the temperature profile simulated by using finite-element-method software Flow 3D (<http://www.flow3d.co.jp/>). The experimental measurement of TE properties is carried out and analyzed in chapter 4. The effects of Nb substitution on TE properties as well as DFT calculations are carefully discussed. Chapter 5 highlights the work and future study.

Chapter 2

Synthesis of $\text{Mo}_{1-x}\text{Nb}_x\text{S}_2$ single crystals

2.1 Introduction

Because the aim of this research is to fabricate and investigate TE properties of the devices of ultrathin layers Nb-doped MoS_2 , the quality of these ultrathin layers becomes crucial. To synthesize the single crystals of Nb-doped MoS_2 with high purity and crystallinity, I use the CVT method, a technique proposed by Schäfer [56, 57]. The CVT method summarizes heterogeneous chemical reaction which is based on the principle that a condensed phase, generally a solid, is able to be volatilized and deposited elsewhere in the form of crystals in the presence of a gaseous reactant. Then micromechanical exfoliation [58, 33] is applied to extract the ultrathin layers. In my synthesis, in order to get the large and high-quality single crystals, a series of parameters consisting of temperature of the chamber, the temperature difference between the hot and cold side, the size of the ampoule, and the growth time are optimized. These optimized parameters also meet the demand for growth of single crystals that were proposed by Nitsche *et al.* [59-61].

This chapter presents the optimal procedure to synthesize single crystals of MoS_2 , $\text{Mo}_{0.99}\text{Nb}_{0.01}\text{S}_2$, $\text{Mo}_{0.98}\text{Nb}_{0.02}\text{S}_2$, and $\text{Mo}_{0.97}\text{Nb}_{0.03}\text{S}_2$. The XRD analysis combining with micromechanical exfoliation of ultrathin layers suggest the successful synthesis of the single crystals and the fabrication of ultrathin layers of Nb-doped MoS_2 .

2.2 Synthesis of $\text{Mo}_{1-x}\text{Nb}_x\text{S}_2$ single crystals

2.2.1 Preparation of clean quartz ampoules

All my quartz tubes used for the CVT growth of single crystals typically have the inner diameter of 8.8 mm and the wall thickness of about 1 mm. Firstly, the diamond saw cut the quartz tube into shorter ones with 50 cm in length. Then the heater (oxy - acetylene flame)

was used to melt the center of the tube and cut it into two equal ones with 25 cm in length. At the distance of 10 cm from the opposite open-ended side of the tubes, the diameter was made narrower into 3 mm as shown in figure 2.1. All contaminants inside and outer of quartz ampoules were removed by burning around the ampoules with the flame.



Figure 2.1 Quartz ampoules used for the CVT growth of single crystals.

2.2.2 Introduction of the powdered materials and transport agent into quartz tubes

To synthesize single crystals of MoS_2 , $\text{Mo}_{0.99}\text{Nb}_{0.01}\text{S}_2$, $\text{Mo}_{0.98}\text{Nb}_{0.02}\text{S}_2$, and $\text{Mo}_{0.97}\text{Nb}_{0.03}\text{S}_2$, the stoichiometric amount of powder materials of Mo, Nb, S and I_2 as a transport agent having the following purities (%) Mo 99.99, Nb 99.9, S 99.99 and I_2 99.9 as shown in Table 2.1 were introduced into the ampoule by using the scale (BP 210 D Sartorius) with high accuracy. For safety, 400 mg of S was chosen. In my synthesis, the molar ratio $n\text{S}/(s\text{Mo} + n\text{Nb}) = 2.05/1$ is best. A slightly excess amount of S was introduced into the ampoule to compensate for the evaporation of S (0.05) due to the heating. This does not influence the Nb substitution because the stability calculation has revealed that the substituted Nb atoms are stable at the Mo sites but unstable at the S sites [54]. The concentration of the transporter I_2 was chosen about 10 mg/ml of the ampoule's volume for all compositions.

Furthermore, to minimize the evaporation of I_2 and S during heating, the powders were poured into the ampoule following the order: I_2 , S, Mo and Nb (figure 2.2). After introducing the powders, again the oxy-acetylene flame was used to make narrower the narrow-necked part of ampoule down to 1mm in diameter as seen in figure 2.3.

Table 2.1 Amount of powder materials for synthesis by using CVT method

Composition	Mo (mg)	S (mg)	Nb (mg)	Ampoule's volume (ml)	I ₂ (mg)
MoS ₂	583.86	400		8.7	87
Mo _{0.99} Nb _{0.01} S ₂	577.95	400	5.65	8.71	87.1
Mo _{0.98} Nb _{0.02} S ₂	572.18	400	11.31	8.71	87.1
Mo _{0.97} Nb _{0.03} S ₂	566.27	400	16.96	8.73	87.3

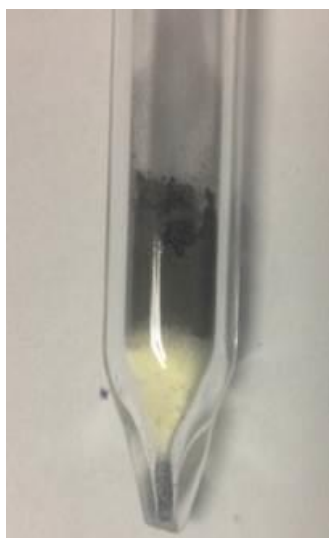


Figure 2.2 Powders were introduced into ampoule following the order: I₂, S, Mo, Nb.



Figure 2.3 Narrow-necked part of ampoule.

2.2.3 Sealing off the ampoules

The prepared ampoule was soon connected vertically to the gauge port of the vacuum system and waited for high vacuum reaching to 3.10^{-6} Torr. When the vacuum reached to 10^{-5} Torr, liquid nitrogen was used for cooling down the ampoule to prevent the sublimation or vaporization of the iodine. When the evacuation was sufficient, the ampoule was melted slowly and sealed uniformly at the narrow neck by the oxy- acetylene flame. After sealing off, the uniform of the ampoule thickness was checked by optical microscopy to avoid the explosion when putting it into the electric furnace at high temperature.

Before putting the evacuated ampoule into the electric furnace, the ultrasonic was used about 15 minutes to make the uniform mixture of powders inside the ampoule (figure 2.4).



Figure 2.4 Uniform mixture inside the evacuated ampoule.

2.2.4 Synthesis

The sealed quartz ampoule was then put in an electric furnace for growth. The heater power of the electric furnace generated a gradient temperature in order to provide the CVT reaction inside the ampoule. The suitable temperature difference between the hotter and the colder ends was pre-measured by using a thermocouple. The temperature distribution inside the furnace tube in my experiment was measured by thermometer when the maximum temperature reaching up to 1050 °C as shown in figure 2.5.

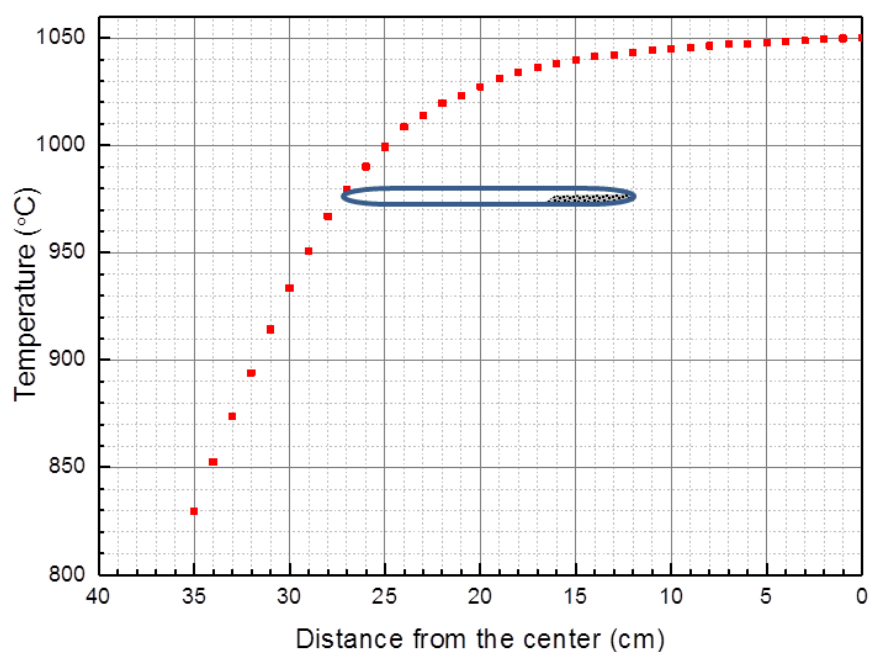


Figure 2.5 Temperature distribution inside the furnace tube.

To avoid any explosion because of the strongly exothermic reaction and the high volatility of S, the evacuated ampoule was slowly heated with the rate about 1°C per min, from room

temperature to 1050 °C for 19.5h. The heating period for synthesizing the single crystals was about two weeks. In my experiment, the condition for synthesis was listed in table 2.2.

The time dependence of temperature inside the furnace tube was controlled as figured out in figure 2.6. At high-temperature region T_H , the powders and transport agent were volatilized in the form of a chemically intermediate phase. The intermediate phase then diffused or converted to the lower temperature region T_L . Finally, that phase decomposed and deposited single-crystals according to the following equations:



Table 2.2 The condition for synthesis

Composition	$T_H (^{\circ}\text{C})$	$T_L (^{\circ}\text{C})$
MoS ₂	1045	1000
Mo _{0.99} Nb _{0.01} S ₂	1045	1000
Mo _{0.98} Nb _{0.02} S ₂	1045	985
Mo _{0.97} Nb _{0.03} S ₂	1045	985

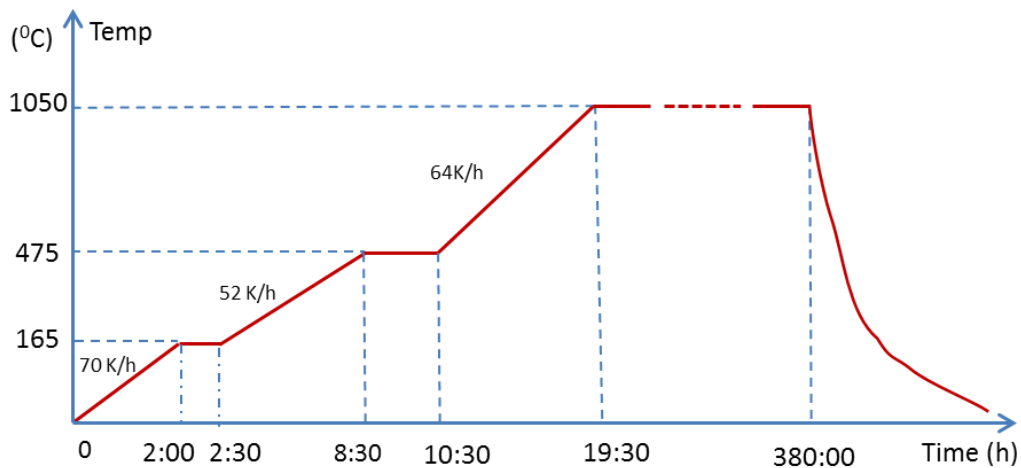


Figure 2.6 The period for synthesis of single crystals.

2.3 Results and discussion

After two weeks of synthesis, the cooled quartz ampoules were carefully taken out the electric

furnace. A diamond disc blade machine was used to cut the quartz ampoules for taking out the grown crystals. Then the grown crystals were rinsed with ethanol to remove the iodine and remaining sulfur condensed on the crystals. The results indicate the thin and shiny crystals with high crystallinity. Figure 2.7 shows photographs of some crystals grown in my experiment. All most crystals have the hexagonal shape similar to the hexagonal crystal structure of transition metal dichalcogenides. The synthesized flakes with hundred μm -size in diameter and μm -size in thickness obviously confirm the anisotropy of growth rate (plate shape). Also, some big flakes with mm in diameter were synthesized (figure 2.8).

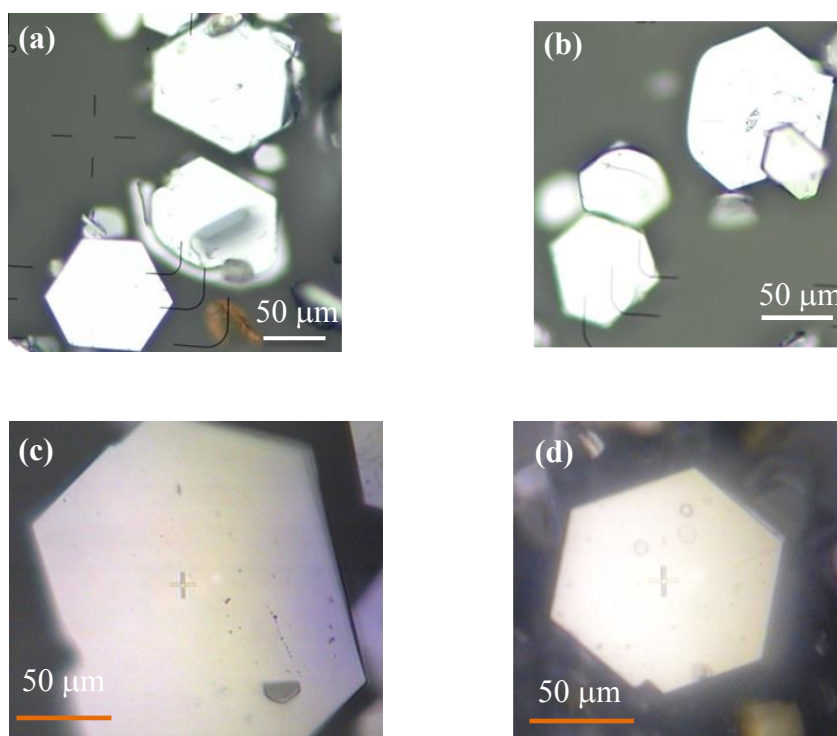


Figure 2.7 Single crystals of grown materials by CVT method.
(a) MoS₂, (b) Mo_{0.99}Nb_{0.01}S₂, (c) Mo_{0.98}Nb_{0.02}S₂ and (d) Mo_{0.97}Nb_{0.03}S₂.

By using the XRD analysis, the XRD pattern and Miller indices were calculated as shown in figure 2.9. The results give a good agreement with those of reported 2H-MoS₂ [62]. The obtained lattice constants are also consistent with those of reported database of MoS₂ as shown in table 2.3.

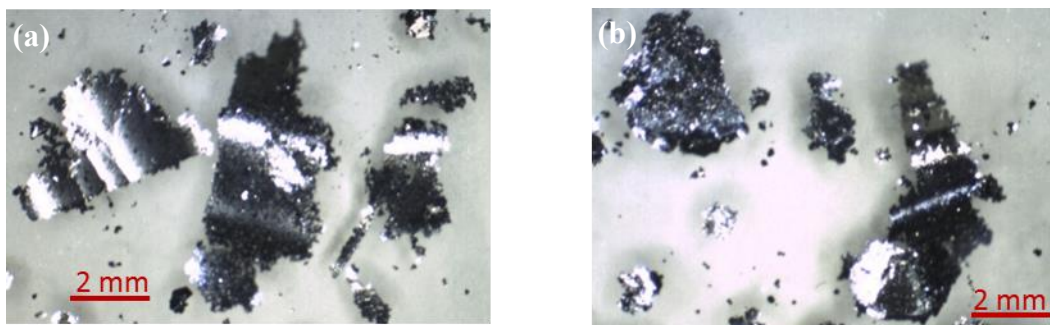


Figure 2.8 Big flakes of (a) MoS_2 and (b) $\text{Mo}_{0.97}\text{Nb}_{0.03}\text{S}_2$.

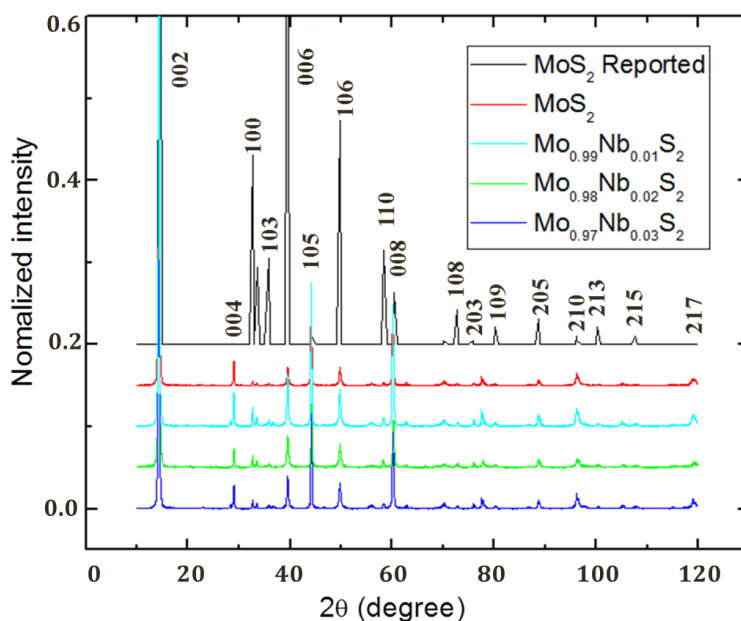


Figure 2.9 The XRD pattern and obtained Miller indices of MoS_2 , $\text{Mo}_{0.99}\text{Nb}_{0.01}\text{S}_2$, $\text{Mo}_{0.98}\text{Nb}_{0.02}\text{S}_2$, $\text{Mo}_{0.97}\text{Nb}_{0.03}\text{S}_2$ and reported MoS_2 .

Furthermore, in the next section, by using mechanical exfoliation to isolate ultrathin layers, it will support for evidence that the synthesized materials are single crystals.

As can be seen from the table 2.3, all values of $x = 0, 0.01, 0.02$ and 0.03 of Nb substitution, a single phase derived from MoS_2 is obtained. Furthermore, MoS_2 and NbS_2 have the same 2H crystal structure and similar lattice parameters, with $a = 0.316$ and 0.332 nm and $c = 1.229$ and 1.194 nm, respectively [63, 64]. Mo and Nb atoms have the similar covalent radius with 130 pm and 134 pm in sequence and their oxidation states in the 2H-polytype lattice are nearly identical. Furthermore, no impurity peaks of Nb are shown in the

X-ray diffraction pattern of Nb-doped MoS₂ samples. The lattice constants of MoS₂, Mo_{0.99}Nb_{0.01}S₂, Mo_{0.98}Nb_{0.02}S₂ and Mo_{0.97}Nb_{0.03}S₂ bulk samples are found to be quite similar (table 2.3), which confirms the small amount of substitution of Mo by Nb in MoS₂ bulk crystal without affecting the lattice parameter. To determine the stoichiometry of Nb-doped MoS₂, Energy Dispersive X-ray Spectrometry (EDS) or Secondary-Ion Mass Spectrometry (SIMS) is conventional use. However, EDS's sensitivity is not enough in this case (Nb is only 3%). In contrast, SIMS has a good sensitivity, but this is a destructive inspection. If we use X-ray fluorescence analysis with wavelength dispersive type, a few % of Nb may be able to detect semi-quantitatively. However, this can be evidenced by indicating the p-type degenerate semiconductor in chapter 4.

Table 2.3 Lattice parameter of synthesized single crystals and reported database MoS₂

	a = b (nm)	c (nm)
MoS ₂	0.3163 ± 0.0002	1.233 ± 0.001
Mo _{0.99} Nb _{0.01} S ₂	0.3163 ± 0.0002	1.230 ± 0.001
Mo _{0.98} Nb _{0.02} S ₂	0.3165± 0.0002	1.229± 0.001
Mo _{0.97} Nb _{0.03} S ₂	0.3166± 0.0002	1.224 ± 0.001
Reported MoS ₂ [62]	0.3161	1.2298
Reported MoS ₂ [63]	0.316	1.229
Reported NbS ₂ [64]	0.332	1.194

2.4 Micromechanical exfoliation and atomic force microscope

The large ultrathin layers obtaining from mechanical exfoliation can give the evidence for confirming the single crystal phase of the synthesized material. The micromechanical exfoliation was carried out by applying a piece of scotch-tape to the surface of a synthesized single crystal and peeling off about 10 times. The tape was then deposited on the pre-cleaned SiO₂/Si substrate and carefully peeled back by applying force parallel to the substrate surface to minimize adhesive residue (figure 2.10 (a)). The ultrathin layers identified by the optical

microscope (figure 2.10 (b)) and measured its thickness by using the atomic force microscope (AFM) (figure 2.11). The uniform thickness about 2 nm (3 layers) of the ultrathin layer with few μm in length and width supports the layered structure of the single crystals. In addition, 3 layers of $\text{Mo}_{0.97}\text{Nb}_{0.03}\text{S}_2$ achieved from AFM convince us that the scotch tape method is effective for fabricating the devices of ultrathin layers.

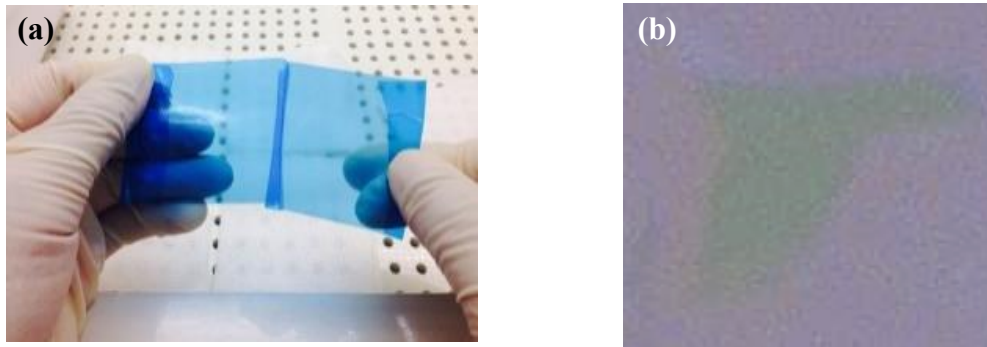


Figure 2.10 (a) Ultrathin layers are isolated by mechanical exfoliation and (b) transferred onto SiO_2/Si substrate.

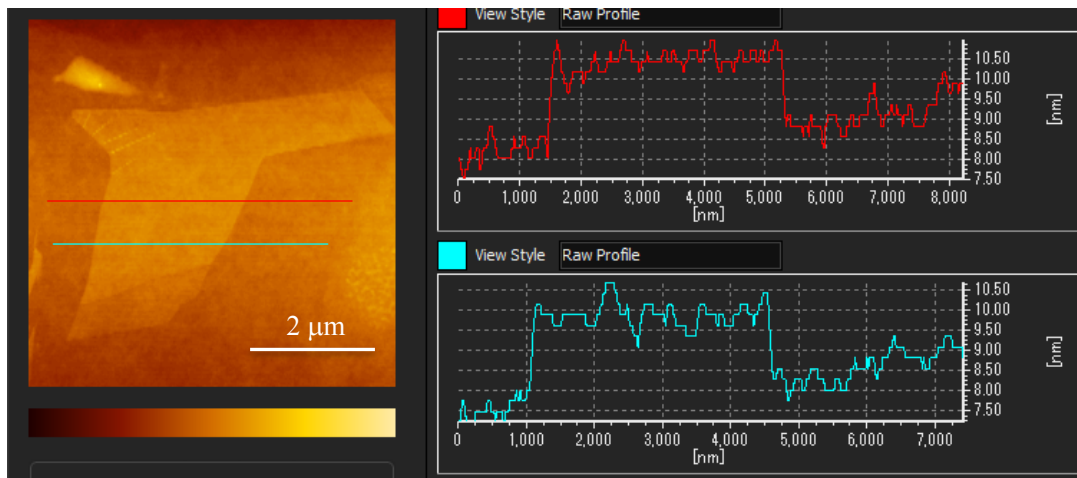


Figure 2.11 AFM measurement of thickness of ultrathin layer of $\text{Mo}_{0.97}\text{Nb}_{0.03}\text{S}_2$.

2.5 Conclusion

The CVT growth technique for synthesizing $\text{Mo}_x\text{Nb}_{1-x}\text{S}_2$ ($x = 0, 0.01, 0.02, 0.03$) single crystals has been successfully applied. This is a reliable method for growing single crystals of transition metal chalcogenides. The ultrathin layers of Nb-doped MoS_2 achieved from

mechanical exfoliation confirm not only the layered structure of synthesized materials, but also the evidence for the growth of single crystals. The ultrathin layers will be used to produce the devices for investigating TE properties in next chapters.

Chapter 3

Device fabrication of ultrathin layers of Nb-doped MoS₂

3.1 Introduction

The performance of TE devices based on two-dimensional (2D) layered crystals of transition metal dichalcogenides in general, and Nb-doped MoS₂, in particular, is significantly affected by electrical and thermal contacts between electrodes and these materials [65]. In fact, the major issue for 2D devices is the existence of a large contact resistance at the interface due to Fermi level pinning effect and the inconsistency of work function [66] between the material and deposited metals, which drastically suppresses the electrical and thermal current in the device. Therefore, along with fabrication technique to form nanostructures, the proper choice of deposited metals to improve the electrical and thermal conduction at the contacts is very important for performing reliable and repeatable measurements of TE properties.

Since ultrathin layers of Nb-doped MoS₂ show p-type semiconducting behaviour, the good interface between the sample and deposited metal requires suitable materials with high work function, such as Au, Pt, and Ni. Among these materials, Au is chosen because of its chemical stability and good electrical conduction [29, 67, 68].

In this chapter, I report a reliable method to fabricate the devices of ultrathin layers of Nb-doped MoS₂ for investigating TE properties. This model is also supported by the device simulation of the temperature profile.

3.2 Design of device fabrication of ultrathin layers

The device fabricated in this study is shown schematically in figure 3.1. According to this scheme, the 100nm SiO₂/heavily doped n-type Si substrate with pre-markers is spin-coated with methyl methacrylate (MMA) and polymethyl methacrylate (PMMA) in sequence (figure 3.1(a)). In order to fabricate the thermometers, first EBL is used to draw the two small

rectangular holes with $1\mu\text{m}$ in width and $2\mu\text{m}$ in length paralleled each other. These exposed patterns are developed by the solution of methyl isobutyl ketone (MiBK) and isopropyl alcohol (IPA) and rinsed by IPA (figure 3.1(b)). Then, the substrate is submerged into buffered hydrofluoric acid (BHF) and rinsed by deionized water to totally etch and remove the SiO_2 area under the exposed areas (figure 3.1(c)). After that, the patterns of electrodes for the four-probe measurement and the heaters are drawn by the EBL and developed by MiBK and IPA with the same condition (figure 3.1(d)). The substrate with the patterns is put in the chamber for deposition with the thickness of Ti/Au (5/120 nm). Fine and sharp electrodes are obtained after removing all remaining resists by using acetone (figure 3.1(e)). Finally, the ultrathin-layer of Nb-doped MoS_2 is transferred onto electrodes (figure 3.1(f)).

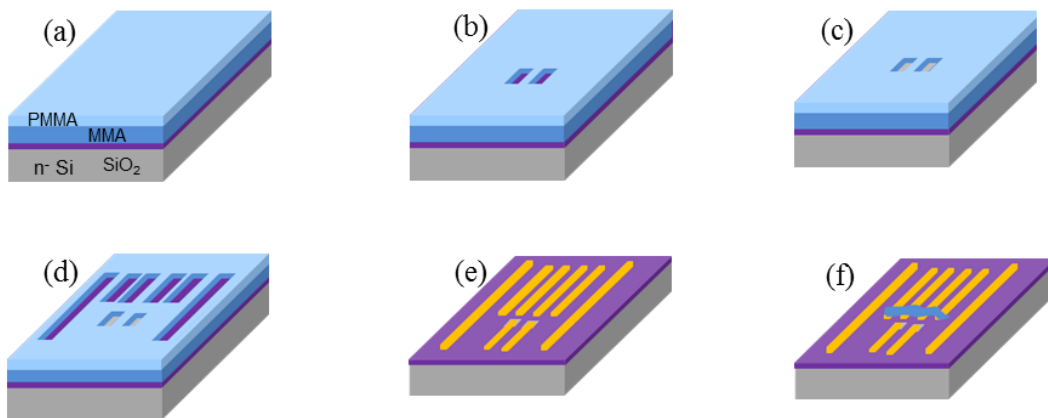


Figure 3.1 Schematic structure of the device for measurement of ρ and S .

3.3 Fabrication the patterns of markers

3.3.1 Preparation of clean substrates

The heavily doped n-type Si/(100nm SiO_2) substrates with $2\text{ cm} \times 2\text{ cm}$ in size were cut by diamond pen from the commercial 4-inch n-type SiO_2/Si wafer. Then these substrates were cleaned in sequence by acetone in 5 mins, IPA in 2 mins, and deionized water in 5 mins with ultrasonic. After that, they were dried by the strong flow of N_2 gas. Finally, the remaining organic contaminants on the substrates were removed by O_2 plasma ashing (15 W, O_2 flowing rate 30 sccm, 5 mins).

3.3.2 Spin coating and electron beam lithography

In principle, EBL is operated by using the focused beam of electrons generated from a scanning electron microscope (SEM) to scan and break cross-links in a resist layers covering on top of the substrate in the desired patterns. Then the exposed areas of resists are removed by using developers. In my experiment, the pre-cleaned Si substrates were coated with MMA 8.5 MAA EL9 and copolymer and PMMA in sequence by using pipettes. The substrates were spin-coated at 4000 rpm for 60 s [69] and then annealed for 5 mins on a hot plate at 180 °C to evaporate the remaining solvents. After cooling down for 60 s, the thickness of MMA/PMMA was about 350 nm/150 nm.

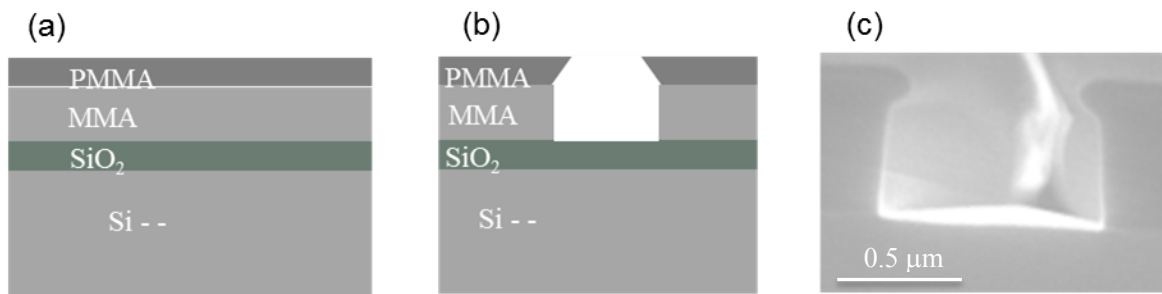


Figure 3.2 Schematic and experimental images for EBL and development.

(a) MMA/PMMA are spin-coated on substrate. (b) Undercut after development.

(c) SEM for undercut observation.

To give the periodic matrix of markers with each field 500 μm x 500 μm in the area, the patterns were designed by using Design AutoCAD LT software. For making a good alignment and reducing error, the size of the marker was 08.μm x 3.2 μm and the distance between two successive markers was 50 μm. When the design was complete, the focused beam of electrons from the EBL was used to draw the patterns in the resist. To make sure that the exposed resist was not under/overdeveloped, the exposure did have to be controlled carefully. For the resist coating utilized in this research, the optimal dose time and electron currents were 5s and a 150pA.

After that, the exposed patterns were developed by the solution of MiBK and IPA with ratio 1:1 in 60 s and rinsed by IPA in 30 s followed by the slow flow of N₂ gas for drying. To

remove the remaining exposed resists on the drawn patterns O₂ plasma ashing (15 W, O₂ flowing rate 30 sccm, 5 min) was used. The process is illustrated in figure 3.2. The fine and sharp undercut of the drawn patterns checked by optical microscopy and SEM confirms the success of the development. The EBL instrument used in this work is ELIONIX ELS 3700 EBL available at clean room 6 (CR6), Center for Nano Materials and Technology (CNMT), School of Materials Science, JAIST.

3.3.3 Deposition and lift-off

Ti/Au metals deposited on the patterned Si substrates were carried out using a thermal deposition system, in which the resistive heating was used to evaporate the atoms of deposited metals from a solid source. These evaporated atoms travelled across the high vacuum chamber and deposited on the substrate, which was connected to a water-cooled plate. Multiple metals with 5nm Ti/30nm Au were deposited sequentially as figured out in figure 3.3(a). The role of Ti is to make a good adhesive on the SiO₂/Si substrate, meanwhile, Au is used for these markers because it is chemically stable in air. Furthermore, the discrepancy in atomic number between Au and SiO₂ produces high enough contrast for us to observe clearly the markers under the resists [70]. This is also important for alignment when using EBL to draw exactly the position of the expected patterns on the substrates.

After the metals were deposited, the resists and the extra metals were removed. The lift-off process was completed in the following steps. First, the device was submerged in hot acetone (60° C) for 1 h to dissolve the resists MMA/PMMA and break up the surface of the undesired metals. The ultrasonic was then used for 30 s to remove all unexpected resists remaining on the substrate, leaving only the patterned metals on the surface. After that, the substrate with markers was put into IPA with ultrasonic in 2 mins to remove acetone. Next, deionized water was utilized to remove IPA in 5 mins. The substrate was dried by a strong flow of N₂ gas. Finally, the organic contaminants on the substrate were removed by using O₂ plasma ashing

(30 W, O₂ flowing rate 30 sccm, 5 mins). The images of SEM for observation the deposited metals and experimental markers after lift-off are shown in figure 3.3(b) and figure 3.3 (c).

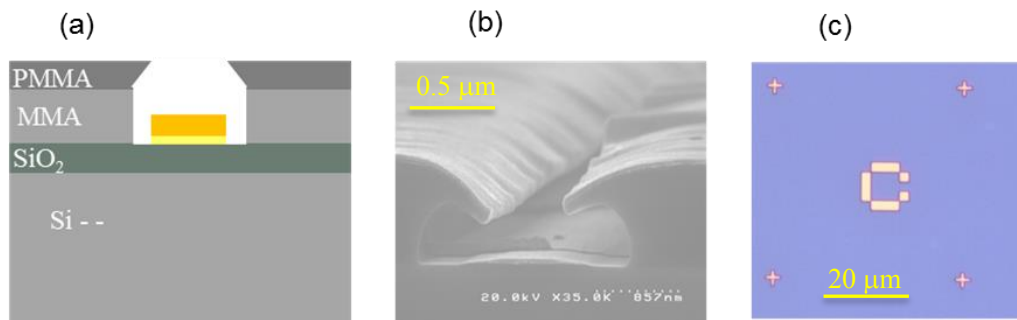


Figure 3.3 Schematic and experimental images for deposition and lift-off. (a) Ti/Au deposited on the exposed area. (b) SEM for observation the deposited metals. (c) Experimental markers after lift-off.

3.4 Fabrication of electrodes for transferring ultrathin layers

From the substrate with the pre-marker patterns, electrodes were fabricated with two times of using EBL for alignment. First, repeating the optimal conditions mentioned above from spin coating to development, we drew the two small rectangular patterns with the size 1 μm in width and 2 μm in length. The black ground colour in figure 3.4(a) confirms the real surface of the SiO₂ layer. Then the substrate was submerged into buffered hydrofluoric acid (BHF) solution 16.6% in 80 s and rinsed by DI water to totally etch and remove the SiO₂ area with 100 μm in thickness under the exposed patterns as shown in figure 3.4(b). In my experiment, the white colour of the etched areas indicated that the wet etching was successful (figure 3.4(c)).

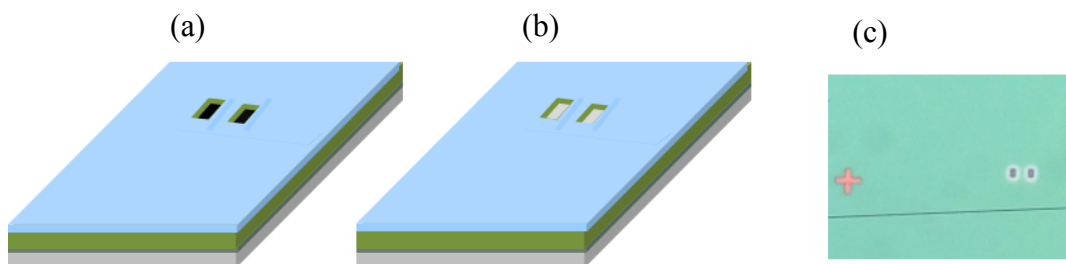


Figure 3.4 Schematic and experimental images for etching by using BHF. (a) Exposed area after development. (b) Exposed area after etching. (c) Experimental area after etching.

The substrate was drawn by using EBL for the second time to expose the electrode patterns. After developing, an optical microscopy was used to check the sharpness of the patterns and the connection between the etched areas and electrodes. Good alignment confirms the continuity between the etched areas and electrodes (figure 3.5(a)). Before carrying out the thermal deposition, wet etching by using important BHF solution 16.6% was conducted to remove the thin layer of SiO₂ because of oxidization when putting the substrate in air. However, the time for etching was just 3s to ensure only SiO₂ layer in the rectangular area exposed in the first exposure to be removed totally. Next, the substrate with the patterns was put in the chamber for thermal deposition. The thickness of the deposited metals depends on the aim of fabrication of the supported layer or suspended layer. For the first time, we fabricated the supporting layer and thus 5nm Ti/120 nm Au metals were deposited on SiO₂/Si substrate. The fine and sharp undercut of the drawn patterns checked by using optical microscopy confirms the success of development and lift-off process (figure 3.5(b)).

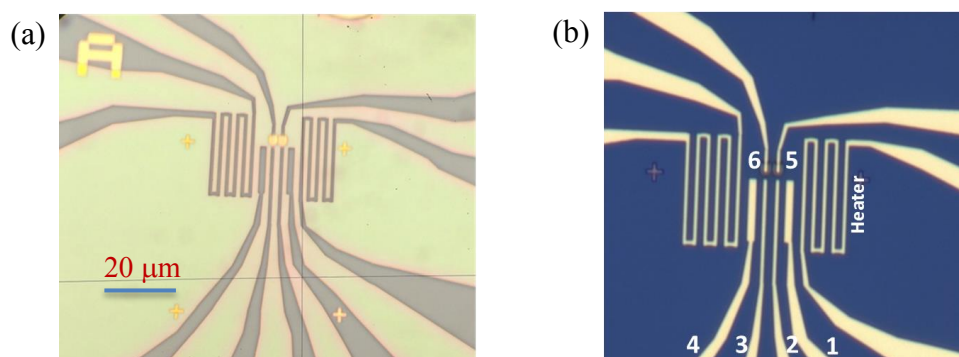


Figure 3.5 Optical images of (a) drawn patterns after development and (b) electrodes after lift- off process.

By fabrication of these heaters with long length and parallel of heater bars, it is believed that temperature gradient through thermometers and sample is nearly uniform.

3.5 Mechanical exfoliation of ultrathin layers and transferring

3.5.1 Checking the electrical status of electrodes

Before transferring the ultrathin layers onto electrodes, the below steps were paid carefully. Firstly, to check the possibility of leakage current between electrodes, a voltage up to 0.5 V

was applied between any couple of electrodes to measure the leakage current. The results showing the ten fA order of currents confirm no leakage current in these electrodes, as illustrated in figure 3.6 for the case of sample # 1. Secondly, the electrical contacts between electrodes 5 and Si substrate, electrode 6 and Si substrate, respectively, were checked by measuring the IV characteristics. In spite of the Schottky barrier between deposited metal Ti and Si substrate, the results presented in figure 3.7 for these samples display the success of etching for making these electrical contacts. This is because the measurement of S does not need the induction of external current, it means open circuit configuration. Finally, any contaminants on the surface of Au electrodes were removed by O₂ plasma ashing (15 W, O₂ flowing rate 30 sccm, 5 min) to increase the electrical contact between sample and Au electrodes.

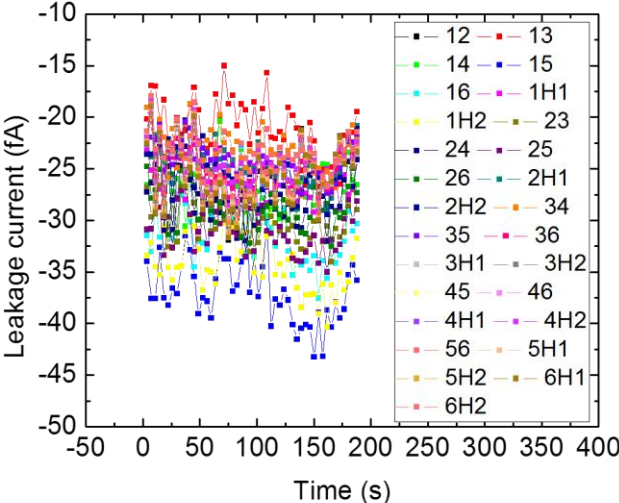


Figure 3.6 Leakage current in sample # 1.

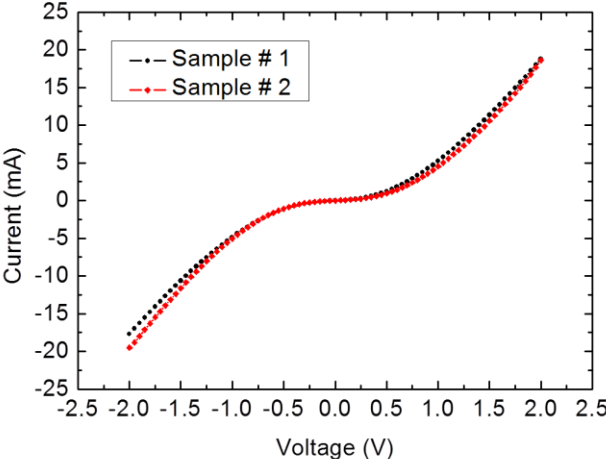


Figure 3.7 IV characteristics between electrodes 5 and 6 for the samples # 1 and # 2.

3.5.2 Preparation of ultrathin layers and transferring

To transfer ultrathin layers onto electrodes, we used the 2D Hetero-transfer system in Mizuta Lab (figure 3.8) called “The Apollo System”. The schematic diagram for isolating ultrathin layers is described in figure 3.9.

First, a pre-cleaned Si substrate with clear markers was covered by soluble water layer – Polyvinyl Alcohol (PVA). Next, the second layer of PMMA was spin coated. Both layers were spun at 5000 rpm in 60 s. Then the Si substrate was baked at 110 °C for 2 mins. After that, thin flake obtained from mechanical exfoliation was transferred onto PMMA layer and peeled off.

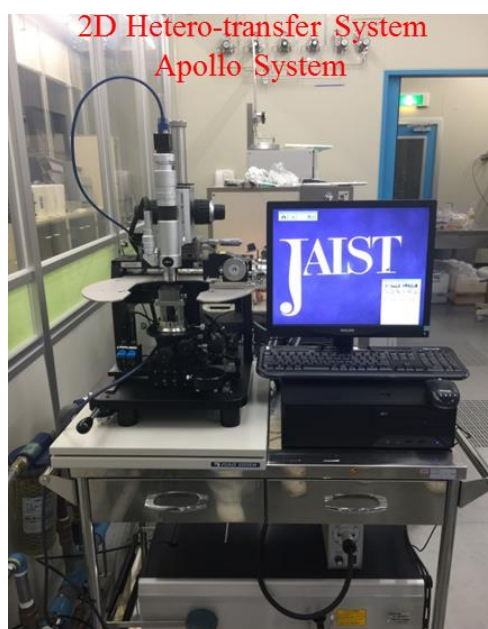


Figure 3.8 The Apollo System for transferring ultrathin layer onto electrodes.

From the observation of the flake’s colour, ultrathin layers on PMMA were collected. After that, the substrate with the ultrathin layers was submerged in hot water to dissolve the PVA layer. The PMMA layer with targeted flakes was then floated on the hot water. Next, a metal slide was used to select the PMMA layer containing the sample and put in the oven for drying.

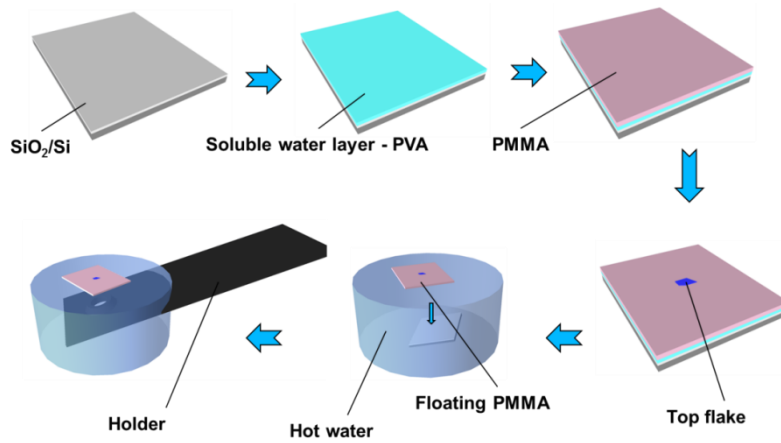


Figure 3.9 The schematic diagram for isolating the ultrathin layers.

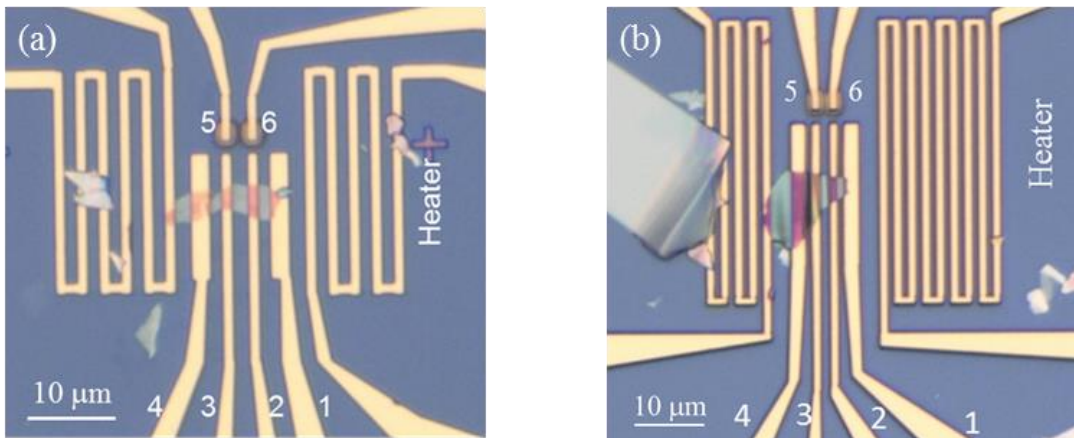


Figure 3.10 Optical images of (a) sample # 1 (b) sample # 2.

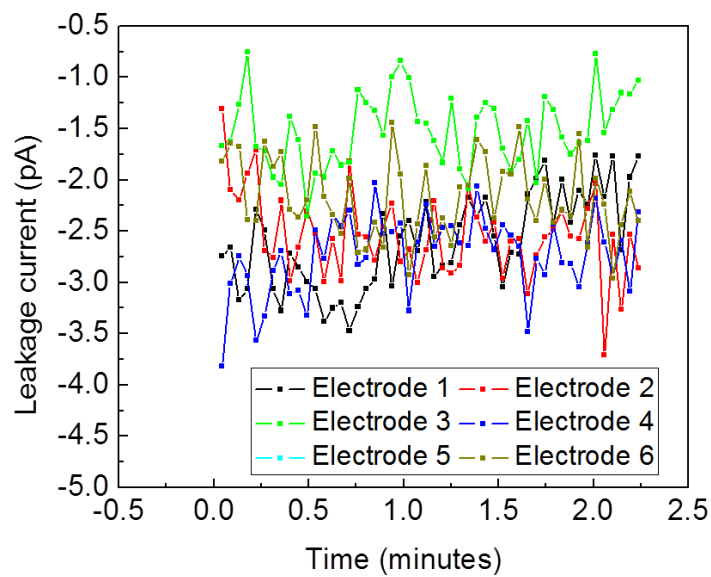


Figure 3.11 Leakage current in sample # 1 when applying a DC current 35 mA in the heater.

Samples on the PMMA layers were transferred onto target electrodes by using the Apollo system. The substrates with samples were immersed for 30 mins in hot acetone (60⁰C) to dissolve PMMA. Finally, the substrates were put on a hot plate (100⁰C) in 10 mins for drying. Figure 3.10 indicates the success of transferring ultrathin layers onto electrodes.

In the measurement of S of these samples, when a current is applied to the heater to generate gradient temperature, it can cause the leakage current through the heater to electrodes. Therefore, I checked the leakage current in each electrode by applying a DC current up to 35 mA to the heater. The results indicate that the leakage current with pA order is negligible. Figure 3.11 shows the case of sample # 1 with a few pA.

According to this scheme, the resistance of the sample is measured by using four-probe method, with 4 electrodes 1, 2, 3 and 4 by applying a DC current through electrodes 1 and 4 then measuring the voltage between electrodes 2 and 3 in open circuit configuration [46, 71]. The two electrodes 6 and 5 connected to Si substrate are used as thermometers. To measure S of the sample, a current is applied to the heater. The temperature gradient is generated and results in the thermally induced voltage between each couple of electrodes 2 and 3, 6 and 5, respectively. The geometry of the heater and the parallel bar electrodes suggest that the temperature difference ΔT between electrodes 2 and 3 is similar to that ΔT_{Si} between electrodes 6 and 5. As a result, the thermal voltage induced ΔV_s between electrodes 2 and 3, and ΔV_{Si} between electrodes 6 and 5 are created, respectively. When the Seebeck coefficient of the Si substrate S_{Si} is measured from PPMS, ΔT_{23} is determined as bellow

$$S_{Si} = -\frac{\Delta V_{Si}}{\Delta T_{Si}}$$

$$\Leftrightarrow \Delta T_{Si} = -\frac{\Delta V_{Si}}{S_{Si}} \cong \Delta T$$

Linear fit from the plotting the relationship between ΔV_s and temperature difference ΔT , S of the sample will be deduced experimentally.

3.6 Device fabrication for measurement of the temperature dependence of S of the heavily doped n-type silicon wafer

To measure the temperature dependence of S of the heavily doped n-type silicon wafer that was used for the substrate of the sample, I used Physical Property Measurement System Thermal Transport Option (PPMS TTO) [72]. The design of the sample is shown in figure 3.12. Here, the two-probe method was applied to measure both the Seebeck voltage and the temperature difference. So, it is important to minimize electrical and thermal resistance at the interface between the leads and the sample. From the design requirement, I fabricated the sample as shown in figure 3.13.

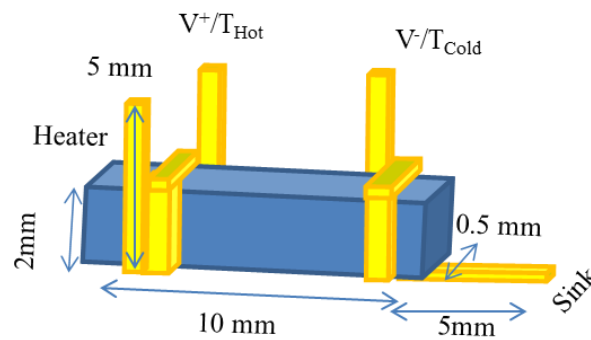


Figure 3.12 The design of device for S measurement.



Figure 3.13 Experimental device for S measurement.

In this device, the measured total resistance of sample about 3Ω is small enough for reducing the effect of the contact resistance. To fabricate this device, I first cut the heavily doped n-type 100 nm SiO_2/Si wafer, which was also used for the substrate in fabricating the

devices of ultrathin layers, with the size 10 mm in length, 2 mm in width, and 500 μm in thickness. Then I polished all its edges by using the rough paper to remove the SiO_2 insulation layer. After that, the Si ingot was tightened by Cu wire and outer covered by Au. Next, I covered the tightened areas by Au paste and Ag paste in sequence to increase thermal and electrical conductivity and adhesion. Then the sample was put on the hot plate (100 $^{\circ}\text{C}$) in 10 minutes for making the mechanical strength of the adhesion. Finally, the sample was installed in TTO puck (figure 3.14).

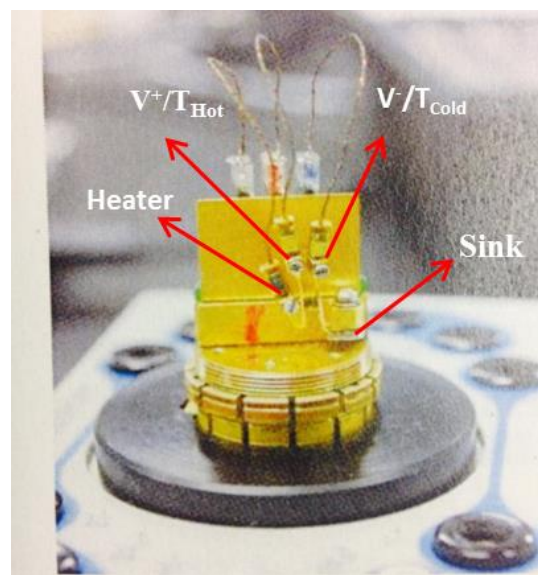


Figure 3.14 Optical image of TTO puck.

3.7 Simulation of the temperature profile

According to the fabricated devices (figure 3.10), my samples were placed on the metal electrodes deposited on SiO_2/Si substrate. As discussed in the previous section, the metal lines 2 and 6, 3 and 5 surrounding the sample parallel to the long metal lines forming the heating structure. This supposes that the temperature difference between electrodes 2 and 3 is similar to that between electrodes 6 and 5. Moreover, because of the very much higher thermal conductance of the large Si substrate compared to that of the thin SiO_2 layer ($d \sim 100 \text{ nm}$) and deposited metals, the heat dissipation in the Si substrate is dominated to generate the temperature gradient when applying the heating current. This means that the sample's

temperature is isothermal with that of the substrate despite the presence of metal lines and the SiO₂ layer. To support this proposal, I have carried out the simulation of the temperature profile, time-evolution of temperature difference, and the discrepancy between the sample and thermometer measurement points by using finite-element-method software Flow 3D (<http://www.flow3d.co.jp/>). My simulated model consists of corresponding parameters of the sample # 1, in which the rectangular heating structure and parallel electrodes all were formed by Au metal and deposited on the 100 nm SiO₂/Si substrate. Their size and position are figured out in figure 3.15. Here, I used conventional thermal quantities for gold, silicon and SiO₂. I assume that the sample thermal conductivity is 1.5 WK⁻¹m⁻¹ because the nanostructured MoS₂ value is unknown. The uncertainty did not give significant changes to the results, because the sample size is smaller than the whole device size. Figure 3.16 shows the constant-temperature line profile surrounding electrodes with the interval of lines 0.5 K. The constant-temperature lines indicate pseudo-spherical profile around the rectangular heater. The patterns neighboring the potential electrodes and thermometers are smooth compared with those near the heater. Figures 3.17 indicates the definition of the temperatures; T_2, T_1 are the temperatures of the sample above electrodes 2 and 3; T_4, T_3 are the temperatures at Au electrodes 6 and 5; T_6, T_5 are the temperatures of the Si surface beneath electrodes 6 and 5; and T_8, T_7 are the temperatures of the Si surface beneath electrodes 2 and 3. All temperatures reached the steady state after 800 sec. When the heater power is 70 mW, the temperature difference between these electrodes ($T_2 - T_1$ and $T_6 - T_5$) is about 1.3 K at the steady state. Figure 3.18 shows the time-evolution of temperatures between the two significant points. At this state, the temperature difference in the sample $T_2 - T_1$ is 1.37 K, meanwhile, the temperature difference of the thermometers which are the junctions of silicon surface ($T_6 - T_5 = 1.24$ K) and Au electrodes ($T_4 - T_3 = 1.27$ K) is 1.255 K. This small discrepancy of 1.37 K and 1.255 K has the possibility to produce an error of 8% for S measurement. The thermal resistance between the sample and the electrode interface is

ignored in this simulation. If the thermal resistance of the two interfaces is the same, the effect will be cancelled by determining the temperature difference.

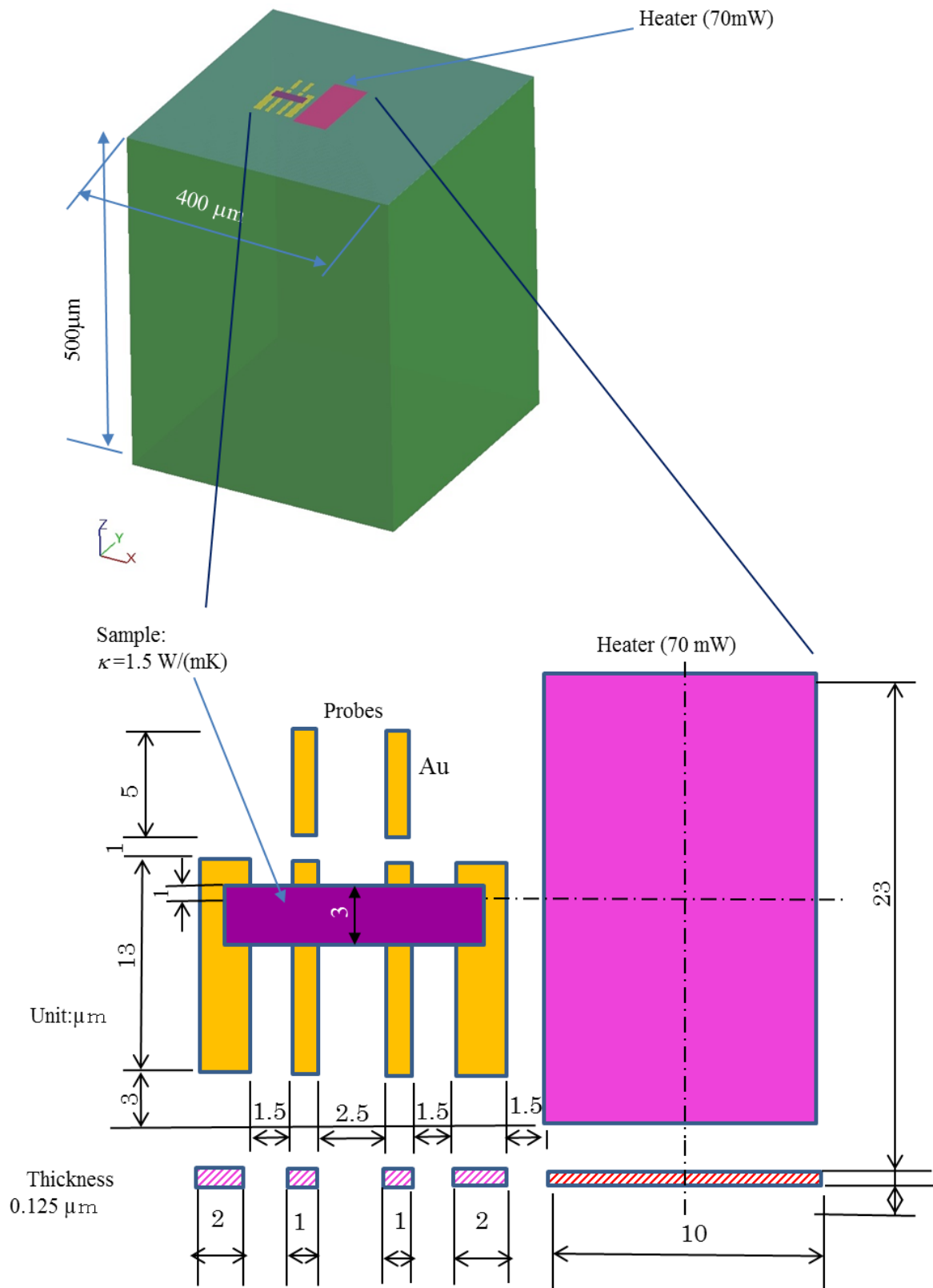


Figure 3.15 The simulated device based on the real device using Flow 3D simulation model.

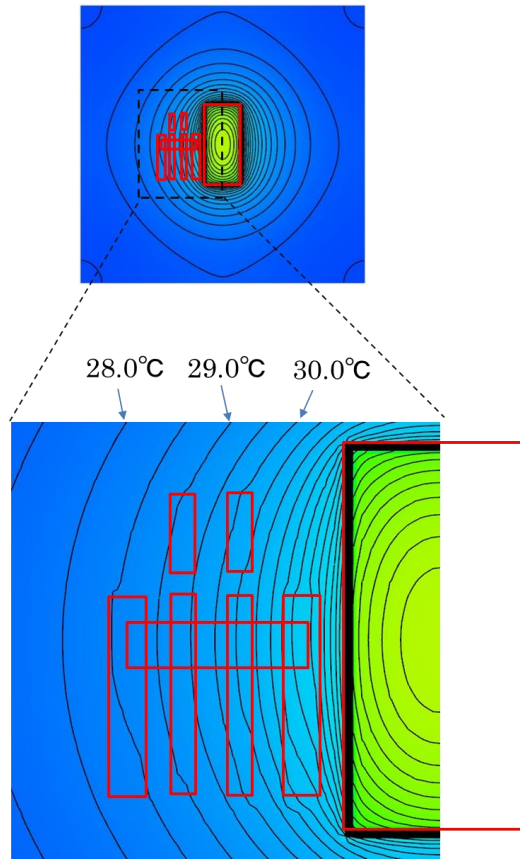
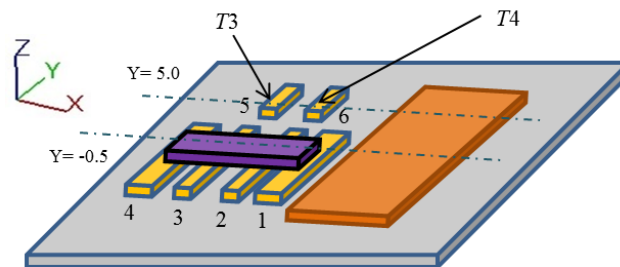
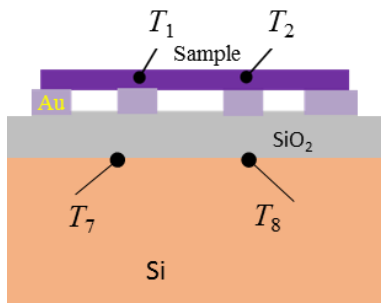


Figure 3.16 The temperature distribution surrounding Au electrodes and the sample.



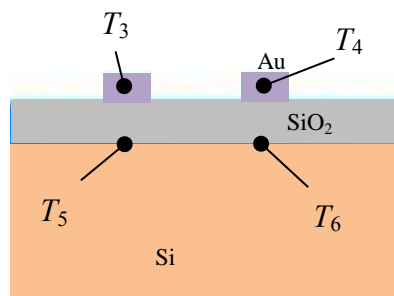
T_1, T_2 : The temperature of the sample above the electrodes 3 and 2.

T_3, T_4 : The temperature at electrodes 5 and 6.



“Y = -0.5” of the XZ cross

T_7, T_8 : The temperature at the Si surface beneath electrode 3 and 2.



“Y = 5.0” of the XZ cross

T_5, T_6 : The temperature at the Si surface beneath electrodes 5 and 6.

Figure 3.17 The temperature measurement points on the device

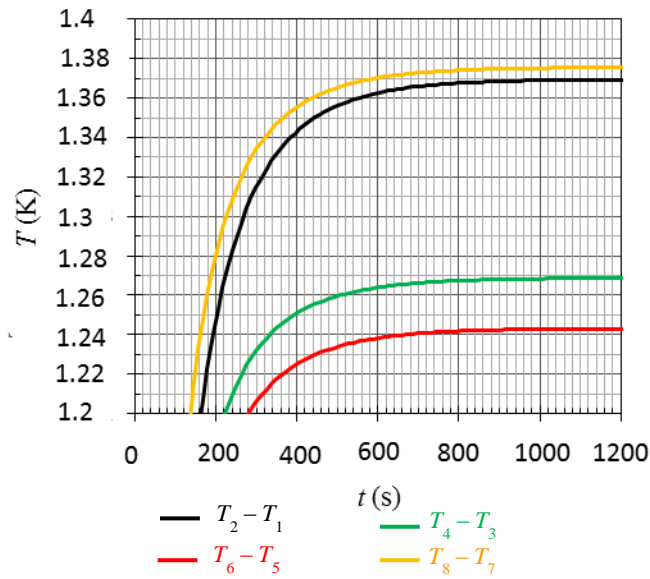


Figure 3.18 Time-evolution of temperatures between the two significant points.

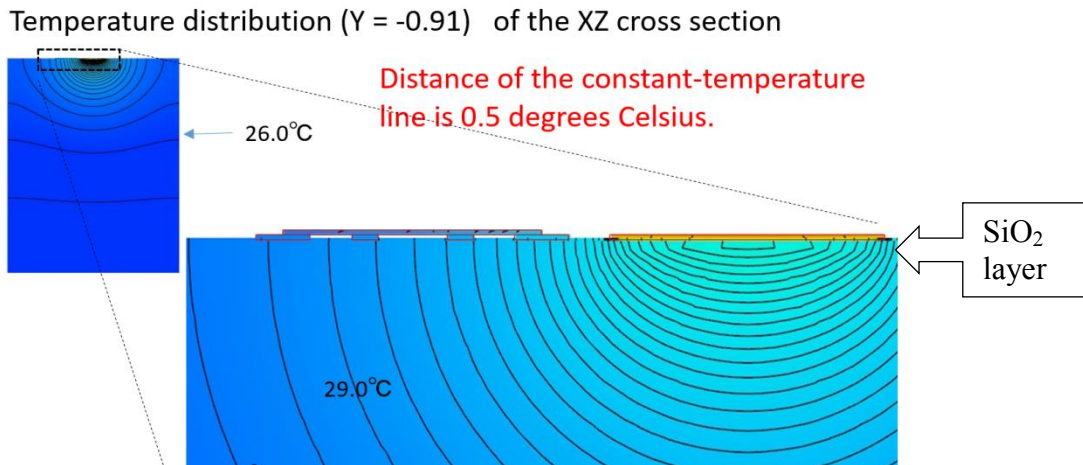


Figure 3.19 The sectional view of the simulated temperature profile.

Figure 3.19 shows the sectional view of the simulated temperature profile. Because the intersection of constant-temperature lines is 0.5 K, I cannot see the difference of 0.005 K or 0.03 K. The constant-temperature lines show a semi-spherical shape in the Si substrate. I can find the effect of the SiO₂ layer in the magnification picture. The bending of the line can be observed at the SiO₂/Si interface at the bottom of the heater. The reason of this bending is the extreme temperature gradient between the high-temperature heater and Si substrate, even in the thin 100 nm thickness. On the other hand, the lines are smooth around the bottom of the sample and electrodes, because of the comparatively gentle slope of the temperature gradient.

3.8 Conclusion

In summary, two devices of ultrathin layers of Nb-doped MoS₂ have been designed and fabricated successfully. This type of structure has been suitable for measuring electrical resistivity ρ by two-probe and four-probe methods and the Seebeck coefficient S . Sharp and fine electrodes, and the negligible leakage currents in these devices were checked carefully to confirm the success of fabrication. Electrical contacts between electrodes 5 and 6 with the Si substrate play the role as thermometers for determining the temperature difference in the sample. This device structure is also supported by the simulation of the temperature profile.

Furthermore, the device of the Si substrate has been prepared productively for measurement of its Seebeck coefficient by using PPMS that supports the measurement of S of samples. The measurement of ρ and S is conducted in the next chapter.

Chapter 4

Results and Discussion

4.1 Introduction

In this chapter, I report on the investigation into the TE properties and effects of Nb dopants on TE transport of two ultrathin layers of Nb-doped MoS₂ based on the measurement of the temperature dependence of their electrical resistivity ρ and the Seebeck coefficient S within the range from 300K to 450 K. I used both two-probe and four-probe methods to measure the contact resistance and sample resistance. The decrease of ρ with rising temperature indicates the semiconducting behaviour of these ultrathin layers. ρ decreases with increasing temperature because of the weak localization and carrier scattering of the conduction carriers by random potential originated from stacking faults and edge roughness.

In the measurement of S , I first measured S of the Si substrate by using PPMS. The result supported the reference to the temperature difference between electrodes 6 and 5, that are played as the thermometers (figure 3.10), after measuring the Seebeck voltage of the Si substrate produced by this temperature difference. From the device fabrication, S of the sample was then deduced from the ratio of the Seebeck voltage induced by the temperature difference between electrodes 2 and 3 to the temperature difference between electrodes 6 and 5. The positive sign of S does not change with the layer thickness. Moreover, the increase of S with rising temperature supposes the p-type degenerate semiconducting behaviour of these ultrathin layers. The experimental results are also consistent with DFT calculation for DOS of pristine MoS₂ and Nb-doped MoS₂ monolayers.

4.2 Measurement of S of heavily doped n-type Si

I measured the temperature dependence of S of heavily doped n-type Si wafer by using PPMS in the chosen temperature range from 240K to 340 K as plotted in figure 4.1. The negative

value of S confirms that electrons are responsible for charge transport heavily doped n-type Si. Also, the enhancement of this absolute value with increasing temperature figures out the degenerate semiconducting behavior of heavily doped Si [73, 74]. Because of the maximum temperature in PPMS measurement just about 340K, to measure S at the higher temperature, I applied the extrapolation of the linear temperature dependence of S on the temperature region from 240 K to 340 K. The formula was deduced as below

$$S_{\text{Si}}(T) = -0.628T - 33 \quad (4-1)$$

Based on the equation (4-1), I extrapolated the value of S at the temperatures higher than 340 K. All the measured values are shown in table 4.1. These values are consistent with those of heavily doped semiconductors [75, 76] and the foundation for estimating S in ultrathin. These values are also consistent with those of layers of Nb-doped MoS₂ mentioned later.

Table 4.1 Temperature dependence of S of heavily doped Si

300 (K)	-220.2 ± 1.3 (μV/K)
315	-229.7 ± 1.4
330	-240.2 ± 1.4
360	-259.1
375	-268.5
390	-277.9
420	-296.8
450	-315.6

4.3 Measurement of ρ and S of ultrathin layers

I used the system called Keithley 4200 CSC in Mizuta Lab with the vacuum system and heater power to measure the temperature dependence of ρ and S of samples # 1 (figure 3.10(a)) and # 2 (figure 3.10(b)) between electrodes 2 and 3.

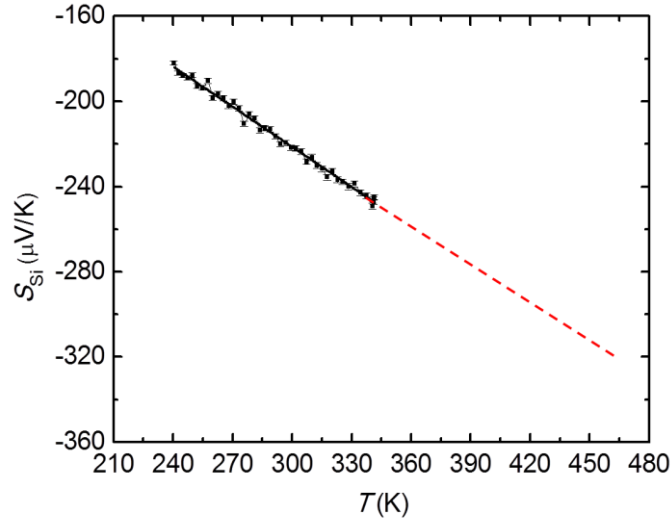


Figure 4.2 Temperature dependence of S of heavily doped n-type Si.

4.3.1 Measurement of ρ

Electrical and TE transport measurements of my devices were performed in an evacuated cryostat, with pressure around 10^{-5} mbar. The IV characteristic of my samples between electrodes 2 and 3 was investigated from 300 K to 450 K. I first measured ρ of sample # 1 with 4.5 nm in thickness (figure 3.10(a)) and sample # 2 with 8 nm in thickness (figure 3.10(b)). I then checked the IV characteristics of these samples by the two-probe and four-probe method. The linear dependence of the IV characteristics of two methods and the overlap between them suggests the ohmic contact between the samples and electrodes. For instance, figure 4.2 shows the data of sample # 1.

Applying the linear curve of the IV characteristics measured by the four-probe method, the temperature dependence of sample resistance was interpolated. Then I estimated ρ after measuring the size of the samples by using AFM. Figure 4.3 indicates the 3D image, the length and the width of sample # 1. Its thickness about 4.5 nm is shown in figure 4.4. The temperature dependence of ρ is displayed in table 4.2.

The temperature dependence of ρ of sample # 1 plotted in figure 4.5 shows the semiconducting behaviour because ρ decreases with rising temperature.

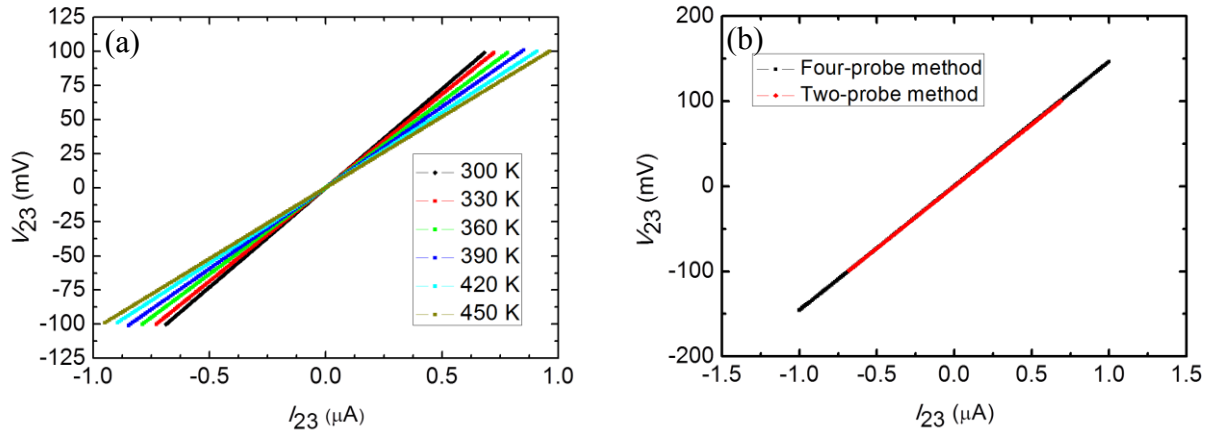


Figure 4.4 (a) Two-probe IV characteristics and (b) overlap of IV characteristics between two-probe and four-probe methods of sample # 1.

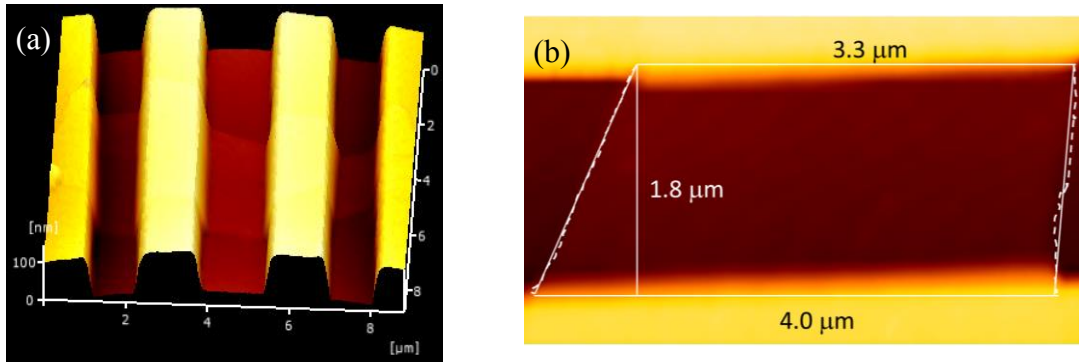


Figure 4.6 (a) 3D image and (b) measurement of the length and the width of sample # 1 by using AFM.

Table 4.2. Temperature dependence of ρ of sample # 1

T(K)	ρ (Ωmm)
300	1.01 ± 0.15
330	0.95 ± 0.16
360	0.87 ± 0.17
390	0.82 ± 0.18
420	0.76 ± 0.19
450	0.72 ± 0.17

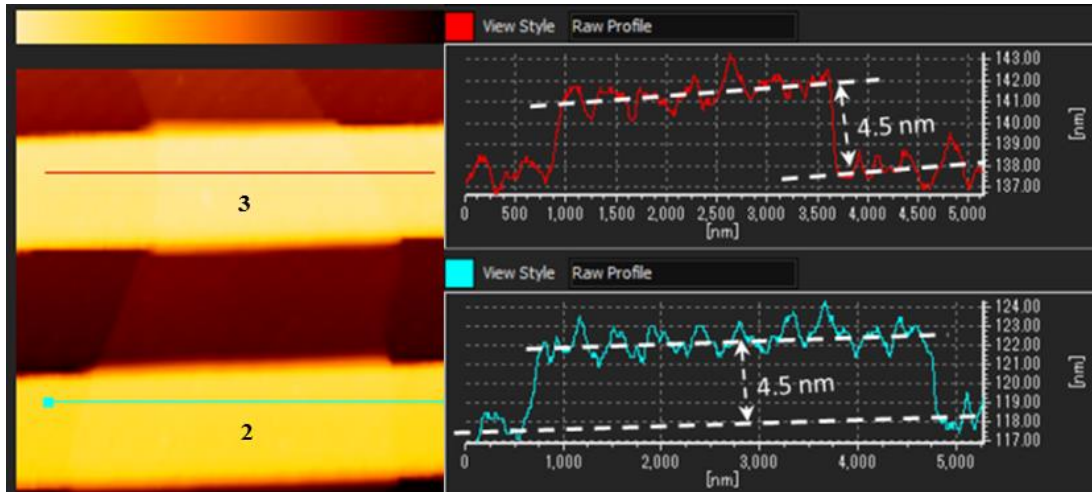


Figure 4.4 Thickness measurement of sample # 1 by using AFM.

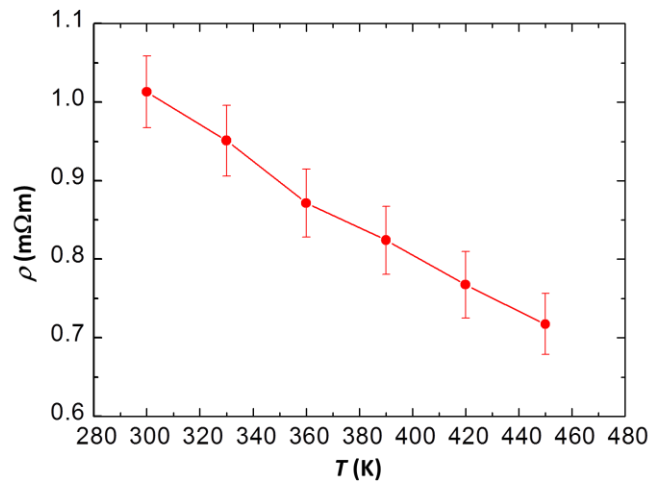


Figure 4.5 Temperature dependence of ρ of sample # 1.

Table 4.3. Temperature dependence of ρ of sample # 2

T(K)	ρ (Ω mm)
300	2.24 ± 0.25
315	2.16 ± 0.25
335	2.08 ± 0.26
355	1.84 ± 0.27
375	1.67 ± 0.24

The temperature dependence of ρ of sample # 1 plotted in figure 4.5 shows the semiconducting behaviour because ρ decreases with rising temperature.

Similarly, I evaluated ρ of sample # 2 after measuring its thickness about 8 nm by using AFM (figure 4.6) and its length and width by using SEM (figure 4.7). The temperature dependence of ρ is displayed in table 4.3 and figure 4.8.

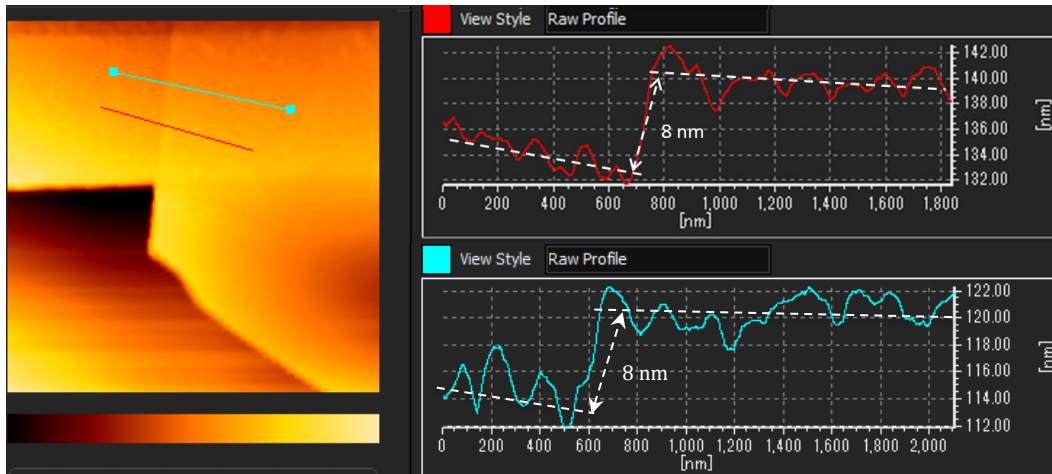


Figure 4.6. Thickness measurement of sample # 2 by using AFM.

Similar to the sample # 1, sample # 2 also shows the semiconducting behaviour. It is noted that the SEM was carried out after measurement of S to avoid the effects of the electron beam of SEM on electrical properties of my samples.

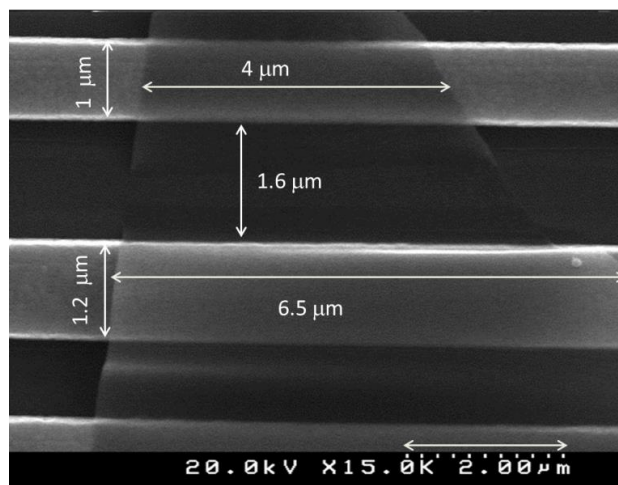


Figure 4.7 SEM image of sample # 2.

Furthermore, I measured ρ and S of the single crystal bulk $\text{Mo}_{0.97}\text{Nb}_{0.03}\text{S}_2$, whose size is $3.6 \times 1.8 \times 0.1 \text{ mm}^3$ by using Agilent 34420A lock-in amplifier and Keithley 2182A nanovoltmeter, these values are $\rho = 120 \mu\Omega\cdot\text{m}$, and $S = 114 \mu\text{V}/\text{K}$ at 300 K, respectively.

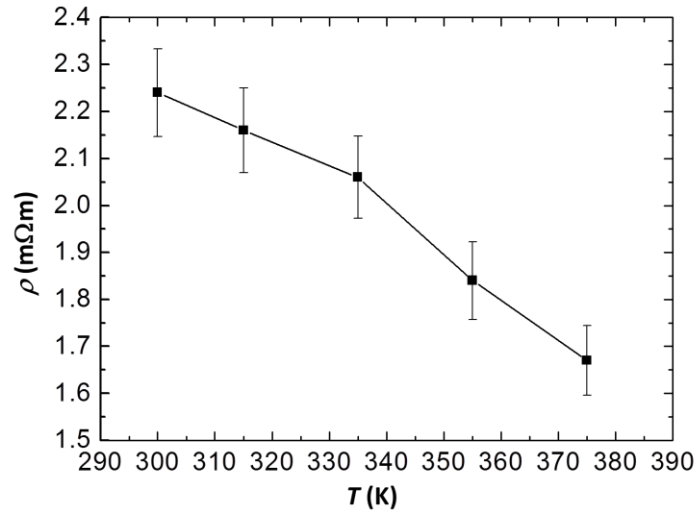


Figure 4.8 Temperature dependence of ρ of sample # 2.

4.3.2 Measurement of the Seebeck coefficient S

After measuring the electrical characterization, the Seebeck effect measurement was carried out. Here I reported on the temperature dependence of the Seebeck coefficient S of sample # 1 from 300 K to 450 K, and that of sample # 2 from 300 K to 375 K. To measure S , a direct current was driven through the heater to create a temperature gradient over sample due to Joule heating. The temperature gradient across electrodes resulted in the Seebeck voltages ΔV , ΔV_{Si} on the sample and the Si substrate between the two couples of electrodes 2 and 3, 6 and 5, respectively. The temperature gradient $\Delta T \cong \Delta T_{\text{Si}}$ across the relevant area was suggested in the previous chapter. S of the sample is, therefore, given by $S = -\Delta V/\Delta T$.

The detailed measurements were carried out as follows. First, a zero current was applied to the heater. The electromotive forces between electrodes 6 and 5 and that between electrodes 2 and 3 were detected in open-circuit configuration. There are the offset values coming from offset currents that were determined from the previous chapter and large impedance of the

machine. Repeating the measurement with increasing heater currents at 10 mA, 15 mA, 20 mA and 25 mA, I obtained the values of the electromotive force of Si and that of the sample depending on the square of heater current. To deduce the Seebeck voltage of the sample and Si, I calculated the mean values of the offset voltage of the sample and Si with 140 μV and 95 μV , respectively. Then I determined the Seebeck voltages of the Si substrate and that of the sample at different heater currents by subtracting the measured voltage from the offset value, respectively. The Seebeck voltages of Si and that of sample linearly increase with increasing square of the heater current.

Because the temperature differences created between electrodes 2 and 3 and between electrodes 6 and 5 are linear with the heater power, this results in a linear dependence of the Seebeck voltage on the temperature difference. Figure 4.9 shows the linear relationship between the Seebeck voltage of Si and that of sample with increasing heater current. This means that the Seebeck effect is effective for both Si and sample. The difference temperature ΔT_{Si} was deduced from the formula $\Delta T_{\text{Si}} = -\Delta V_{\text{Si}}/S_{\text{Si}}$, in which S_{Si} was experimental calculated by PPMS. Next, I plotted the dependence of the Seebeck voltage of sample ΔV on the temperature difference $\Delta T \cong \Delta T_{\text{Si}}$, for example, S of sample # 1 approximated about 128 ± 11 $\mu\text{V/K}$ was interpolated linearly at room temperature, as seen in figure 4.9. The positive value of S confirms that sample displays the p-type semiconducting behavior.

I also measured temperature dependence of thermal conductivity κ of heavy doped n-type silicon substrate used by using PPMS at the same time with S measurement. The experimental data as plotted in figure 4.10 indicate that κ is about $145\text{Wm}^{-1}\text{K}^{-1}$ at 300 K with the error about 5 ~ 10%. This estimated value is much larger than that of the thin layer of SiO_2 ($\kappa_{\text{SiO}_2} \sim 1.1\text{WK}^{-1}\text{m}^{-1}$ [77]) and the deposited metal lines, the heat dissipation in the Si substrate dominates for generating the temperature gradient. This supposes that the sample's temperature is isothermal with that of the Si substrate.

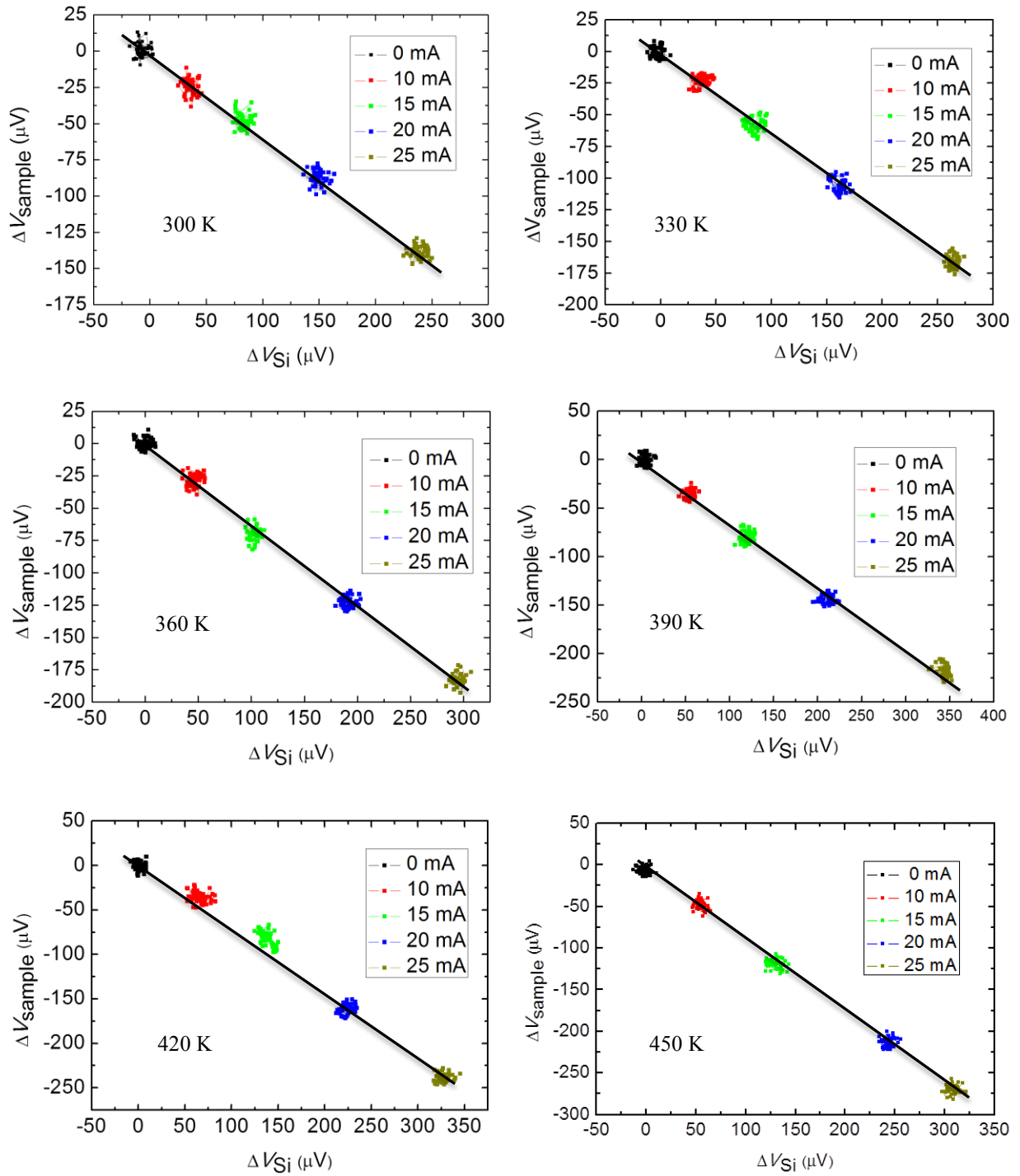


Figure 4.9 The relationship between the Seebeck voltages of sample # 1 and that of the Si substrate at different temperatures.

Repeating the same process for higher temperatures up to 450 K, I evaluated S of the sample #1. The results confirm the linearity between ΔV with ΔT for all measurements at different temperatures as shown in figure 4.11. The temperature dependence of S plotted in figure 4.12 indicates that this quantity increases with rising temperature.

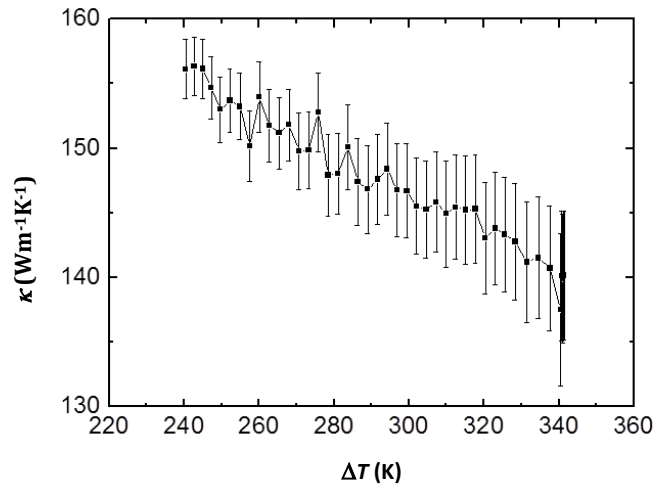


Figure 4.10 Temperature dependence of thermal conductivity of heavy doped n-type Si substrate used.

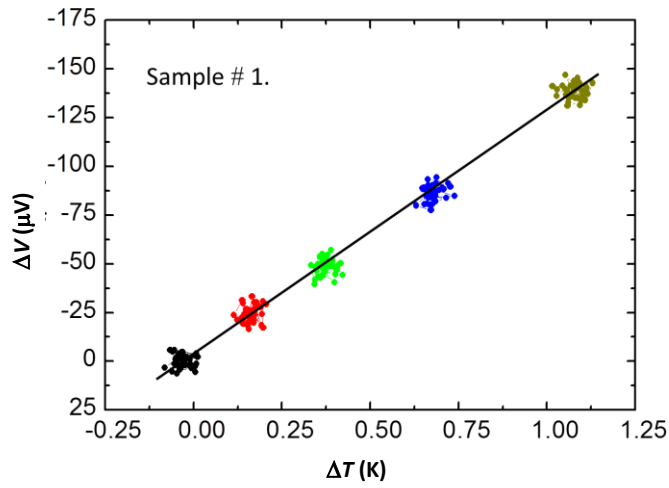


Figure 4.11 Linear relationship between the TE voltage between electrodes 2–3 and the temperature difference measured at electrodes 6–5 at 300 K of sample # 1.

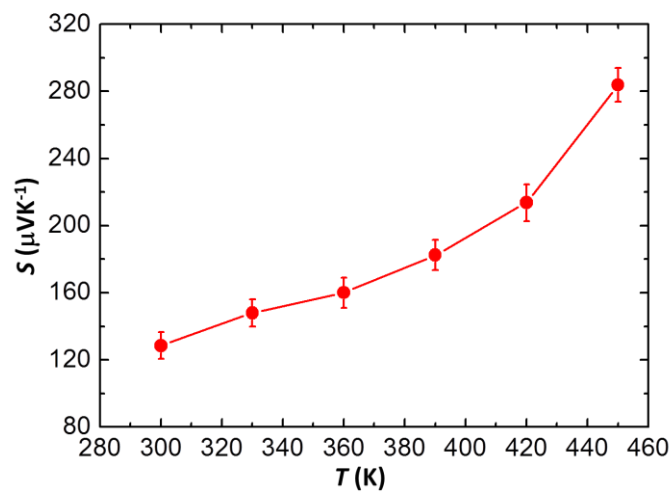


Figure 4.12 Temperature dependence of S of sample # 1

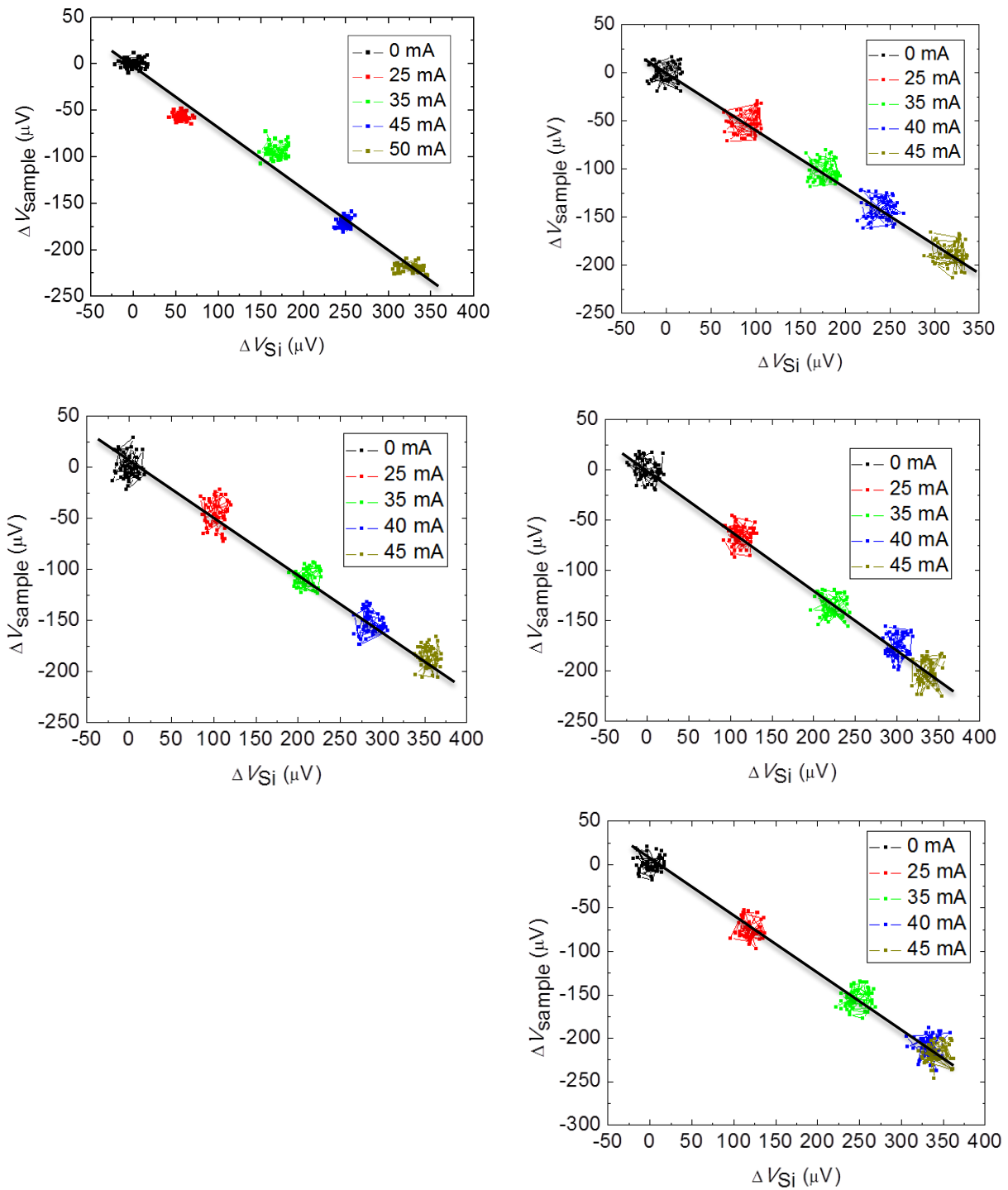


Figure 4.13 Relationship between the Seebeck voltages of sample # 2 and that of the Si substrate at different temperatures.

Similarity, I measured S from 300 K to 375 K with the same condition, for sample # 2. The relationship between the Seebeck voltage of the sample with that of the Si was plotted in figure 4.13. The temperature dependence of S shown in figure 4.14 also indicates the p-type semiconducting behavior of the sample.

Furthermore, I also confirmed the p-type semiconducting behaviour of ultrathin layers Nb-doped MoS₂ by applying a back-gate voltage V_{BG} . The current I_{DS} versus V_{BG} curves were obtained for different values of back gate voltage when maintaining a constant drain-source voltage corresponding to 0.2, 0.4, 0.6, 0.8 and 1 V. As shown clearly in figure 4.15, a more negative back-gate voltage leads to a higher drain current, as it would be expected from a p-type doped semiconductor.

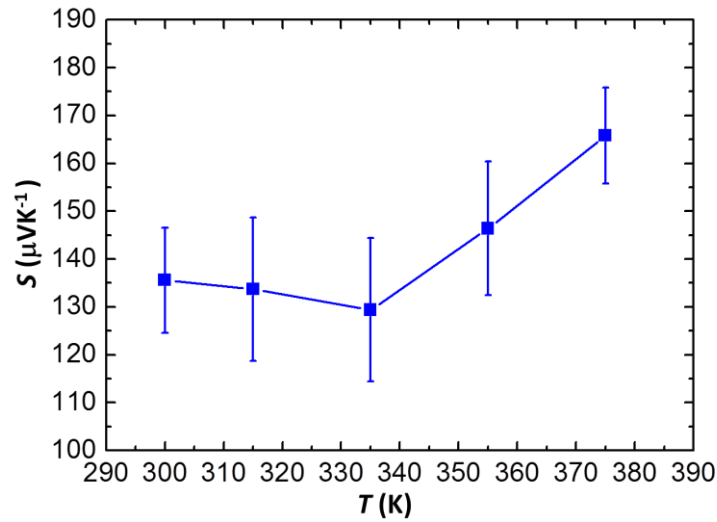


Figure 4.14 Temperature dependence of S of sample # 2.

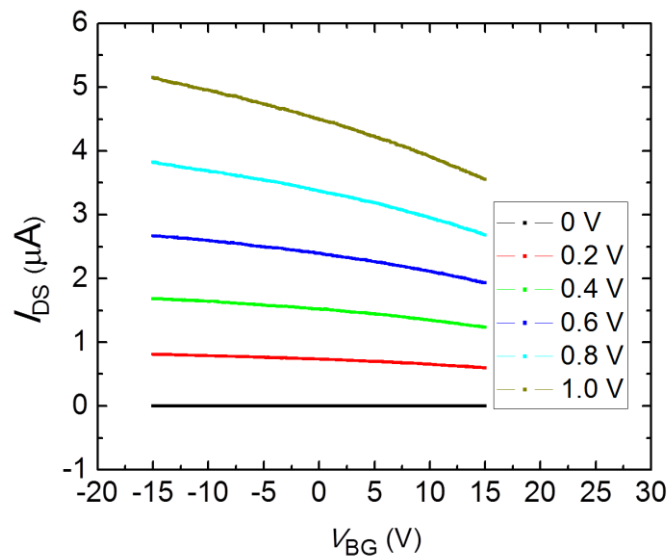


Figure 4.15 Gate voltage dependence of channel current of sample # 1 at a bias voltage from 0 to 1V.

4.4 Discussion

Figure 4.16 displays the temperature dependence of ρ of two ultrathin layers # 1 and # 2 with thicknesses of 4.5 nm and 8 nm, respectively, and a bulk sample at 300 K. The concomitant decrease in ρ with increasing temperature indicates the semiconducting-like behavior of two thin samples. Compared with the bulk sample with $\rho = 120 \mu\Omega\text{m}$ at 300 K, ρ of thin samples is approximately one order larger. This large increase is understood by the carrier localization effect and carrier scattering of the conduction carriers, as explained below.

The temperature dependence of ρ for the two ultrathin samples strongly suggests that the Nb-doped MoS_2 ultrathin layer is not a simple semiconductor because the Arrhenius plot of the ρ - T curve does not follow linear dependence. The conduction carrier system in these samples is considered reasonably as near-2D systems with disorder perturbation.

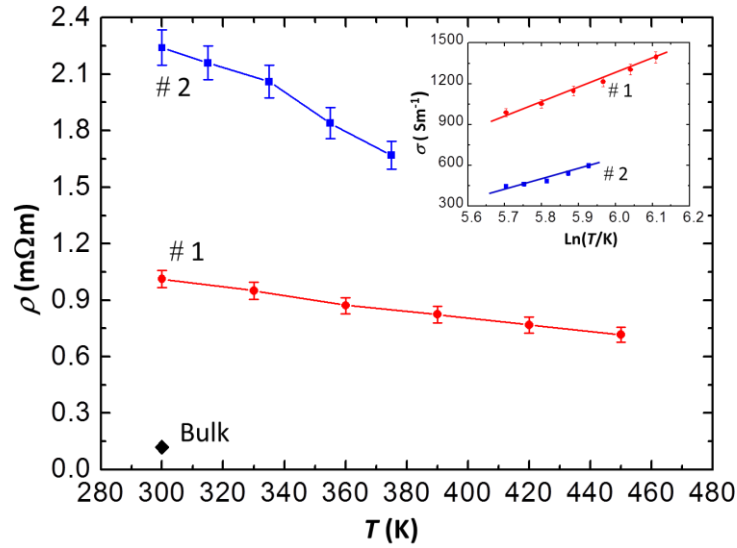


Figure 4.16 The temperature dependence of ρ of two thin samples and bulk at 300 K.

I have considered the models related to the disorder 2D systems, such as variable-range hopping [41, 78], ionized impurity scattering [79], and weak localization [80-82]. In the case of variable-range hopping conduction, the temperature dependence of ρ is given by [80]

$$\rho = \rho_0 \exp\left(\frac{T_0}{T}\right)^{\frac{1}{d+1}} \quad (4-2)$$

where ρ_0 stands for temperature independent constant, T_0 denotes the characteristic hopping energy, and d is the dimension of the electronic system. Furthermore, $d = 1, 2,$ and 3 corresponding to 1, 2, and 3 dimension in sequence. The $\ln\rho - 1/T^{d+1}$ plots of the data portray an unusually large value of T_0 ($k_B T_0 \approx 1eV$). This result suggests the possibility that variable-range hopping conduction is inappropriate.

Regarding ionized impurity scattering, E. Conwell and V.F. Weisskopp [79] evaluated the temperature dependence of ρ as

$$\rho = 2.11 \times 10^2 \varepsilon^{-2} T^{-3/2} \ln\{1 + 36\varepsilon^2 d_{\text{ion}}^2 (kT)^2 q^{-4}\} \quad (4-3)$$

where, d_{ion} is the half of average distance between impurity ions, q is the hole charged carrier and ε is the dielectric constant of the semiconductor. This indicates that ρ due to ionized impurity scattering is affected strongly by $T^{-3/2}$. However, this possibility is rejected by the plot of experimental points.

The weak localization is most suitable for explaining the obtained results. In that case, there are states localized in a tail of the valence band above Fermi level because of the random potential (figure 4.17). The carrier localization has been observed in highly disordered graphene even at room temperature [83, 84]. In my samples, the random potential is the result of the highly disordered system because of Nb substitution, surface defects, and edge roughness. Applying weak localization theory based on Anderson's prediction [80-82] the linear dependence of electrical conductivity σ with $\ln T$ is described as

$$\sigma = \text{const} + (Ce^2/2\pi^2\hbar) \ln T \quad (4.4)$$

where, e represents the charge of an electron, \hbar denotes the reduced Planck's constant, and T signifies the temperature. The inset of figure 4.16 presents the $\sigma - \ln T$ plot of the $\rho - T$ curves. These data exhibit good $\sigma - \ln T$ dependence. This result suggests that the dominant carrier conduction mechanism is weak localization. Basically, electrical conductivity consists of the contribution of weak localization conduction and Drude conduction. In the ground state of

low dimensional (1D or 2D) electron systems, carrier localization state is dominant compared to the Drude conduction by the random potential. With rising temperature, the localized states are broken by thermal excitation of $k_B T$, simultaneously, the electron-phonon scattering suppresses the Drude term. At the higher temperatures like my case, the localization will become weaker and Drude conduction may be dominant. I cannot estimate the ratio of localization and Drude conduction in the current work. In order to evaluate the contribution of weak localization, magnetoresistance measurement at low temperature is effective. If weak localization is dominant, large negative-magnetoresistance will be observed by the breaking of localization bound state.

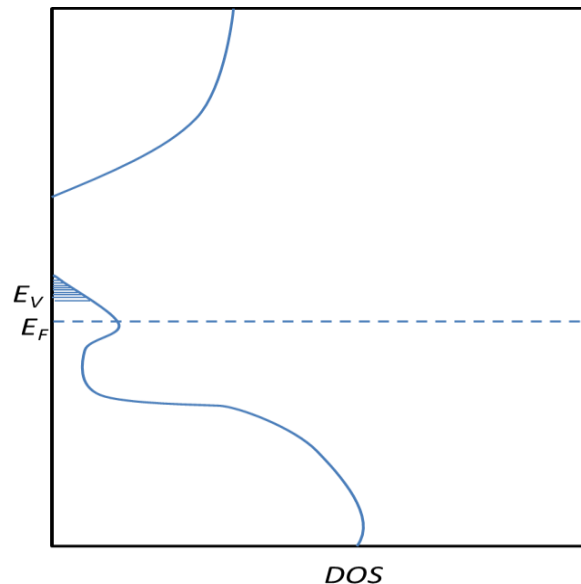


Figure 4.17 DOS consisting of weak (Anderson) localized- states (shaded region). E_F is Fermi level, E_V is mobility edge.

In my sample, the random potential is the result of the highly disordered system because of Nb substitution, surface defects, and edge roughness. With rising temperature, the thermal excitation energy makes these localized states become the conducting carriers leading to an increase in electrical conductivity. One can reasonably infer that the difference between sample # 1 and sample # 2 might include different random potentials. ρ of the thin sample is less than that of the thick sample, which suggests that the strength of localization of sample #

1 is less than that of sample # 2. The probable localization center might be stacking fault or edge roughness, rather than surface scattering or a substrate effect.

Plotted in figure 4.18 is the temperature dependence of the Seebeck coefficient S of the two ultrathin layers and the bulk sample. At 300 K, S of the bulk Nb-doped MoS₂ is not so much different compared to that of ultrathin layers. Based on the Boltzmann theory, S and electrical conductivity σ are given as [85]

$$S = -\frac{1}{eT} \frac{K_1}{K_0}, \quad (4-5)$$

$$\sigma = e^2 K_0, \quad (4-6)$$

where, K_0 , K_1 are defined from the transport coefficient expressed as

$$K_n = \frac{2}{h} \int \Sigma(E, T) (E - E_F)^n \left(-\frac{\partial f_{FD}}{\partial E} \right) dE, \quad (4-7)$$

where, $\Sigma(E, T)$ is the spectral conductivity, E denotes the energy, E_F is the Fermi level, f_{FD} is the Fermi–Dirac distribution function, e is the elementary charge, and T is the electronic temperature. The spectral conductivity $\Sigma(E, T)$ will show a dramatic change if the carrier conduction is changed for some reasons.

According to Boltzmann theory, the electrical conductivity is determined from the spectral conductivity averaged over the very narrow energy range of a few $k_B T$ in width centered at the Fermi level. In ultrathin layers, the localized density of states around the Fermi level due to weak localization become significantly. Moreover, the surface scattering increases in thin samples. Because $\Sigma(E, T)$ consists of the terms of carrier filling in the DOS and relaxation time of carrier scattering, these two factors result in the decrease of electrical conductivity in ultrathin sample compared with that of the bulk sample. In the case of S , the modulation of $\Sigma(E, T)$ by localization effect includes both K_0 and K_1 . The effect of $\Sigma(E, T)$ will be cancelled by K_1/K_0 if the energy dependence of $\Sigma(E, T)$ is not so strong in the range of a few $k_B T$ around E_F . It is consistent with the experimentally obtained result that the obtained S is independent of the thickness, even in a weak localization state.

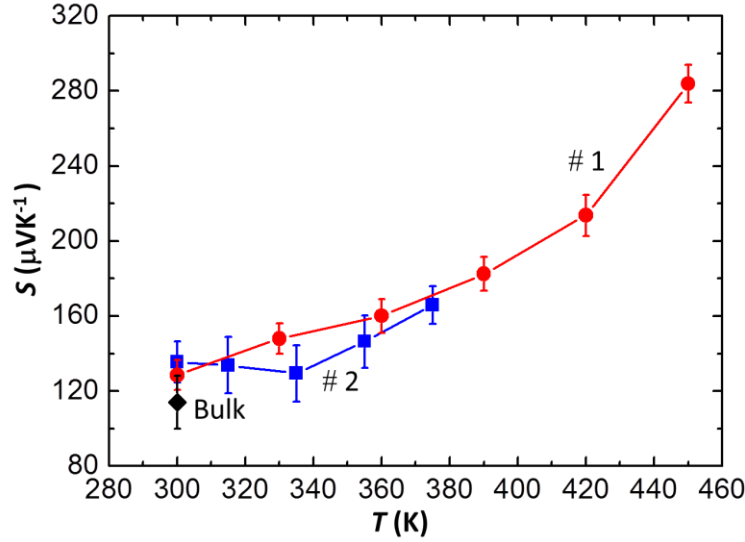


Figure 4.18 Temperature dependence of S of two thin samples, and bulk at 300 K.

The slope of S for both thin samples increases with rising temperature. The slope of the S - T curve from 300 K to 400 K is about $0.6 \mu\text{V}/\text{K}^2$. In general, S consists of two fundamentally independent contributions $S = S_d + S_p$, where S_d presents the diffusion term and S_p denotes the phonon-drag effect [86]. For the measured temperature region, the phonon-drag effect is negligible because the Debye temperature of MoS_2 is lower than 600 K [87]. The diffusion Seebeck coefficient describes the diffusive motion of the charge carrier under the thermal gradient. The diffusive Seebeck coefficient for the carriers is roughly approximated by the Mott relation for a degenerate semiconductor as [23, 86]

$$S_d = \frac{\pi^2 k_B}{3 q} k_B T \left\{ \frac{d[\ln(\sigma(E))]}{dE} \right\} \Big|_{E=E_F} \quad (4-7)$$

where k_B represents the Boltzmann's constant, T stands for the temperature, and the derivative is evaluated at the E_F . Within this approximation, the expression shows the roughly linear dependence of S_d on T , corresponding to the experimentally obtained result portrayed in figure 4.18. The equation (6) is reduced as shown below

$$S_d = \gamma \frac{\pi^2 k_B}{3 q} \frac{k_B T}{E_F} \quad (4-8)$$

That equation is obtained by assuming that $\sigma = C\varepsilon^\gamma$, where C is a constant and γ is the

dimensionless parameter characterizing each scattering process, as in the acoustic phonon scattering case $\gamma = -1/2$ [88]. Using equation (4-8) and the slope of $S - T$ curve in figure 4.19, the roughly estimated value of E_F of the ultrathin layer Nb-doped MoS₂ is about ≈ 30 meV. This value is comparable to the $k_B T \approx 26$ meV to 39 meV, corresponding to thermal energy at 300 K and 450 K; it is not contradictory to the degenerate condition of conduction carriers.

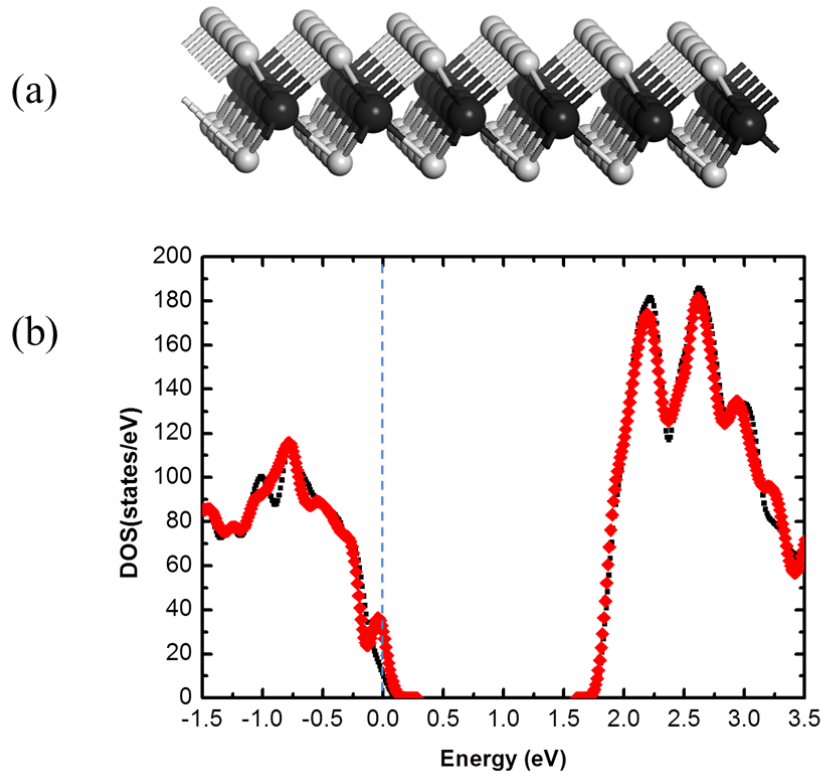


Figure 4.19 DOS for a 6×6 pristine MoS₂ supercell (black line) and a 6×6 MoS₂ supercell in which one Mo atom is replaced by a Nb (red line). The vertical dashed line shows the Fermi level.

To support the explanation of the physical mechanism for electrical and TE transport in the MoS₂ and Nb-doped MoS₂ ultrathin layers, I performed first-principles calculations. A hexagonal monolayer MoS₂ 6×6 supercell (figure 4.19 (a)) with $a = b = 1.897$ nm, $c = 3$ nm, $\alpha = \beta = 90^\circ$, and $\gamma = 120^\circ$ was used for the calculations. The large supercell was employed to prevent the interaction between MoS₂ layers, and between doped size and their periodic images. Nb-doped MoS₂ supercell is built by replacing the Mo atom at the center of the MoS₂

supercell by a Nb atom. All configurations were relaxed to reach minimum-energy structures. DFT calculations [89, 90] were used for calculation. The generalized gradient approximation functional in Perdew-Wang 91 (PW91) [91] form for the exchange-correlation and double numerical plus polarization basis set [92] were used. A $4 \times 4 \times 2$ Monkhorst-Pack grid of k-points was employed for the Brillouin-zone integrations. All calculations were performed using Dmol³ code [93]. The DOS was calculated by Gaussian broadening with the width of 50 meV.

Figure 4.19(b) presents the DOS of the mother material MoS₂ monolayer (black line). The DOS demonstrates a clear band gap E_g about 1.6 eV; it is corresponding to the reported results [94, 95]. It is noteworthy that the Fermi level is located at the top of valence band, not the center of the band gap. The valence band-top consists of the hybridization states of Mo 4*d* and S 3*p* orbitals. The DOS for the Nb substituted MoS₂ monolayer is displayed by the red line in figure 4.19(b). Compared with the pure MoS₂ monolayer, the band does not change. The small DOS peak appears at the top of the valence band because of the hybridization of Nb 4*d* and S 3*p* orbitals. The Fermi level moves to the top of this DOS peak. This movement is consistent with the experimental picture, in which the Nb-doped MoS₂ electronic state is a p-type degenerate semiconductor. The Fermi level estimated from this figure is about 10 meV. It is underestimated compared with the experimentally obtained value about $\mu \approx 30$ meV.

The p-type semiconducting behavior of MoS₂ monolayers in my simulated results is totally different from the early reports of the MoS₂ ultrathin layers in field effect transistor (FET) experiments [40, 41, 50, 51], for which the negative sign of *S* indicates their n-type behavior. This difference suggests the Fermi level pinning at MoS₂-metal interfaces of the source and drain electrodes [66]. At metal–MoS₂ contacts, the interaction between metal and S weakens the intralayer S–Mo bonding and leads to the appearance of the midgap states, mainly of Mo d-orbitals character (figure 4.20). Also, the interface dipole formation because of the charge redistribution results in the modification of work function at the metal side. These interface

effects can have a strong influence on the Fermi level position relative to the valence band maximum and conduction band maximum near the surface [66]. However, in my Nb-doped MoS₂ case, the pinning effect is suppressed strongly because the Fermi level locates into the valence band-top, corresponding to the DFT calculations, as presented by the red line in Figure 4.19 (b).

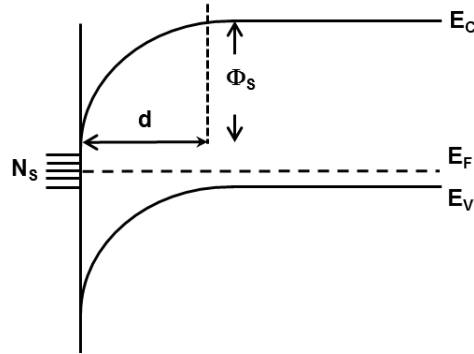


Figure 4.20 Fermi level pinning at energy of the midgap surface states N_s , where d is the depth of space-charge region, and Φ_s is surface potential.

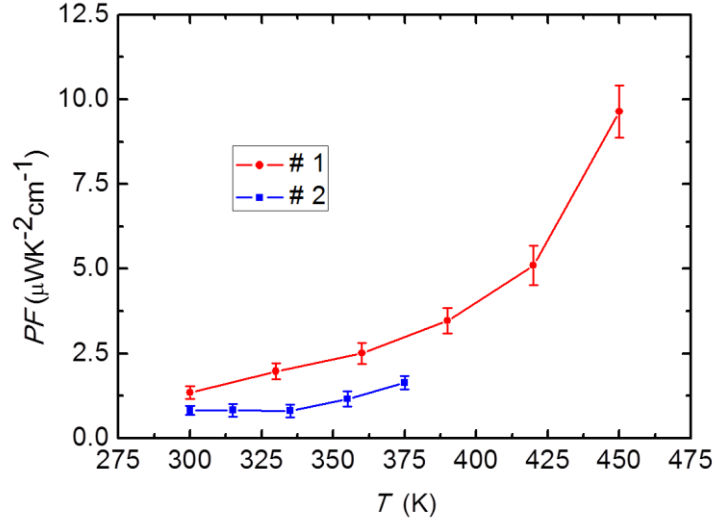


Figure 4.21 Temperature dependence of PF of the sample # 1 and sample # 2.

Figure 4.21 figures out the increase of PF with rising temperature of sample # 1 and sample # 2. My results at 300 K are one order of magnitude smaller when compared to maximum values of PF of n-type MoS₂ bilayers [50, 51]. This is because these values are also dependent on the doped carrier concentration, and the number of layers. In my experiment,

my sample's thicknesses (about 6 layers for sample # 1 and 12 layers for sample # 2) and charged carriers are not the optimum values. However, the high melting point, high-temperature stability, and the rapid increase of PF with rising temperature support the TE potential of this material in the high-temperature region after optimizing the thickness and Nb-doped level.

4.5 Conclusion

In this chapter, I experimentally investigated the TE properties and the effects of Nb dopants on TE transport of the Nb-doped MoS₂ ultrathin layers mechanically exfoliated from my synthesized single crystals. The TE quantities ρ and S were measured over the temperature region from 300 K to 450 K. The experimentally obtained results and DFT calculations indicate that these ultrathin layers are p-type degenerate semiconductors as a result of the suppression of the pinning effect due to Nb dopants. The enhancement of ρ compared to the bulk Nb-doped MoS₂ results from weak localization and carrier scattering of the conduction carriers by random potential originated from stacking faults or edge roughness. This picture is consistent with the decrease of ρ with rising temperature. Moreover, the lack of change of S by layer thickness suggests that the modulation of spectral conductivity $\Sigma(E, T)$ is cancelled even in the localization condition. The experimentally obtained results are also consistent with DOS of pristine MoS₂ and Nb-doped MoS₂ monolayer obtained using DFT calculation. The success of the measurement and the similar tendency of ρ and S of the two samples confirm the reproducibility and reliability of the methodology. The rapid increase of PF at high temperature of this p-type ultrathin layers, that are fundamentally necessary for TE devices consisting of n-type and p-type TE elements, suggests the potential trend for applications in TE nanodevices, like planar Peltier cooling.

Chapter 5

Conclusions and Future Work

In this thesis, I investigate the TE properties of the p-type Nb-doped MoS₂ ultrathin layers that were mechanically exfoliated from my synthesized single crystals of Mo_{0.97}Nb_{0.03}S₂. Based on the temperature dependent measurement of electrical resistivity ρ and the Seebeck coefficient S , and DFT calculations for DOS, this research is the first of a study elucidating the physical mechanism of the influence of the Nb dopants on TE transport properties of p-type Nb-doped MoS₂ ultrathin layers. This research proposes an effective way to fabricate the devices of Nb-doped MoS₂ ultrathin layers in which the Au with high work function, chemical stability, and good electrical conduction makes the good electrical contact with Nb-doped MoS₂ ultrathin layers. Moreover, this research contributes partly to the field of doped ultrathin TE materials, especially offering a tendency for next-generation flexible ultrathin TE materials which suggest the potential for TE applications, like planar Peltier cooling utilized for dissipating the thermal energy generated from nanometer-scale hot spots in the nanodevices.

In detail, this dissertation is divided into 5 chapters and introduces the following important contributions to the field of TE materials. The comprehensive review of TE materials, the working mechanisms of TE devices, the current research and the potential application of 2D materials in TE field are presented in chapter 1. The synthesis of the single crystals Mo_{1-x}Nb_xS₂ obtained by using CVT method with the optimized parameters is presented in detail in chapter 2. The large hexagonal shape, the XRD analysis of the synthesized flakes and smooth ultrathin layers mechanically exfoliated with few nm in thickness that is determined by AFM and SEM measurements confirm not only the single crystalline but also the layered structure of the synthesized compounds.

Chapter 3 presents the process for fabrication of two devices consisting of Nb-doped MoS₂

ultrathin layers and the simulation to justify these devices arrangements. By employing Au electrodes with large work function and high chemical stability for making the contacts with these ultrathin layers, the good electrical contacts measured support the improved thermal contact that has been challenging for nanodevice fabrication recently. The sharp electrodes and the no leakage current between them are reliable for transferring the ultrathin layers onto these electrodes. The reproducibility is confirmed by the reliability and stability of the measurement of the two devices. The good electrical contact between these ultrathin layers and Au electrodes is supported from the overlap between IV characteristics when using two-probe and four-probe methods. This suggests the reliability of the device fabrication and thermal contacts between samples and electrodes that are important for thermal transport and measurement of S of the samples. In addition, by using finite-element-method software Flow 3D, the simulation of the temperature profile shows an error of 8% for temperature difference that is acceptable for thermal transport on the device.

In chapter 4, I experimentally investigate the TE properties of Nb-doped MoS₂ ultrathin layers mechanically exfoliated from my synthesized single crystals. Because the Nb dopants result in the increase of carrier concentration, these ultrathin layers display the p-type degenerate semiconducting behavior in the temperature range from 300 K to 450 K. However, the weak localization and carrier scattering of the conduction carriers by a random potential originated from stacking faults and edge roughness leads to the increase of electrical conductivity of these thin layers when rising temperature due to thermal excitation and the enhancement of their electrical resistivity compared to the bulk Nb-doped MoS₂. Moreover, the independence of S on layer thickness suggests that the modulation of spectrum conductivity is canceled out even in the localization condition. The experimental results are also consistent with DFT calculation for DOS of pristine MoS₂ and Nb-doped MoS₂ monolayers.

This research supposes the deeper understanding of the TE nature in the p-type Nb-doped MoS₂ ultrathin layers. Moreover, the rapid increase of PF at high temperature of this p-type ultrathin layers, that are fundamentally necessary for TE devices consisting of n-type and p-type TE elements, suggests the potential trend for applications in TE nanodevices at the high temperature region. In addition, by increasing the height of the deposited electrodes and using the critical point drier, the fabrication technique in this thesis is useful and reliable for making the suspended structure that is important for the measurement of thermal conductivity [96] by using Raman scattering.

Based on the achieved results, I will progress my research in the future. Firstly, using mechanical exfoliation, I will fabricate the devices with different thickness from single layer to few layers and further investigate the thickness dependence of TE properties and find the largest PF in the wide temperature region. Secondly, by applying the CVT method, I will adjust the amount of Nb substitution and then investigate the effects of the amount of Nb dopants on the TE properties and physical mechanism. Thirdly, by fabricating the suitable height of the deposited electrodes and using the critical point drier to make the suspended structure, I will estimate the thermal conductivity of the Nb-doped MoS₂ ultrathin layers by analyzing the temperature dependent Raman studies of the in-plane E_{2g} and out of plane A_{1g} modes. Carrying out these experiments, I will consider the optimal conditions for fabricating the ultrathin layer that has the largest TE efficiency and deeply understand the physical mechanisms behind the TE phenomena in Nb-doped MoS₂.

Bibliography

- [1] D. M. Rowe, *CRC Handbook of Thermoelectrics*. CRC Press, Boca Raton, 1995, Ch. 1.
- [2] K. Zeb, S. M. Ali, B. Khan, C. A. Mehmood, N. Tareen, W. Din, U. Farid, and A. Haider, A survey on waste heat recovery: Electric power generation and potential prospects within Pakistan, *Renewable and Sustainable Energy Reviews*, **75**, 1142, 2017.
- [3] M. S. El-Genk, H. H. Saber, *CRC Handbook of Thermoelectrics: Micro to Nano* (CRC Press, Boca Raton, 2006), Ch. 43.
- [4] F. J. DiSalvo, Thermoelectric Cooling and Power Generation, *Science*, **285**, 703, 1999.
- [5] S. B. Riffat, X. Ma, Thermoelectrics: a review of present and potential applications, *Applied Thermal Engineering*, **23**, 913, 2003.
- [6] J. P. Heremans, M. S. Dresselhaus, L. E. Bell, and D. T. Morelli, When thermoelectrics reached the nanoscale, *Nature Nanotechnology*, **8**, 471, 2013
- [7] A. F. Ioffe, *Semiconductor Thermoelements, and Thermoelectric Cooling*. Infosearch, Ltd., London, 1957.
- [8] A. J. Minnich, M. S. Dresselhaus, Z.F. Ren, G. Chen, Bulk nanostructured thermoelectric materials: current research and future prospects, *Energy & Environmental Science*, **2**, 466, 2009.
- [9] G. J. Snyder and E. S. Toberer, Complex thermoelectric materials, *Nat. Mater*, **7**, 105, 2008.
- [10] P. Vaquero, A.V. Powell, Recent developments in nanostructured materials for high-performance thermoelectrics, *Journal of Materials Chemistry*, **20**, 9577, 2010.
- [11] X. Zhang, L. D. Zhao, Thermoelectric materials: Energy conversion between heat and electricity, *Journal of Materiomics*, **1**, 92, 2015.
- [12] X. Shi, X. Shi, L. Chen, and C. Uher, Recent advances in high-performance bulk thermoelectric materials, *International Materials Reviews*, **61**, 6, 2016.
- [13] J. F. Li, W. S. Liu, L. D. Zhao, and M. Zhou, High-performance nanostructured

- thermoelectric materials, *NPG Asia Materials*, **2**, 152, 2010.
- [14] J. Yang, Special section papers on thermoelectric materials and applications foreword. *J. Electron Mater*, **36**, 703, 2007.
- [15] J. Yang, T. Caillat, Thermoelectric Materials for Space and Automotive Power Generation. *Mrs Bull*, **31**, 224, 2006.
- [16] H. J. Goldsmid, Bismuth Telluride and Its Alloys as Materials for Thermoelectric Generation, *Material*, **7**, 2577, 2014.
- [17] H. J. Goldsmid, A. R. Sheard, and D. A. Wright, The performance of bismuth telluride thermojunctions, *Br. J. Appl. Phys.* **9**, 365, 1958.
- [18] G.A. Slack, in: M. Rowe (Ed.), CRC Handbook of Thermoelectrics, CRC Press, Boca Raton, FL, 1995.
- [19] Z. G. Chenal, G. Hana, L. Yanga, L. Chenga, and J. Zoua, Nanostructured thermoelectric materials: Current research and future challenge, *Materials International*, **22**, 535, 2012.
- [20] L. D. Hicks and M. S. Dresselhaus, Effect of quantum-well structures on the thermoelectric figure of merit, *Phys. Rev. B*, **47**, 12727, 1993.
- [21] L. D. Hicks, T. C. Harman, and M. S. Dresselhaus, Use of quantum - well superlattices to obtain a high figure of merit from nonconventional thermoelectric materials, *Appl. Phys. Lett*, **63**, 3230, 1993.
- [22] L. D. Hicks and M. S. Dresselhaus, Thermoelectric figure of merit of a one-dimensional conductor, *Physical Review B*, **47**, 16631, 1993.
- [23] M. S. Dresselhaus, G. Chen, M. Y. Tang, R. G. Yang, H. Lee, D. Z. Wang, Z. F. Ren, J. P. Fleurial, P. Gogna, New directions for low-dimensional thermoelectric materials, *Advanced Materials*, **19**, 1043, 2007.
- [24] J. P. Heremans, Low-Dimensional Thermoelectricity, *Acta Physica Polonica A*, **108**, 4, 2005.
- [25] G. R. Bhimanapati, Z. Lin, V. Meunier, Y. Jung, J. Cha, S. Das, D. Xiao, Y. Son, X. S. Strano, V. R. Cooper, O. L. Liang, S. G. Louie, E. Ringe, W Zhou, S. S. Kim, R. R. Naik,

- B. G. Sumpter, H. Terrones, F. Xia, Y. Wang, J. Zhu, D. Akinwande, N. Alem, J. A. Schuller, R. E. Schaak, M. Terrones, and J. A. Robinson, Recent Advances in Two-Dimensional Materials beyond Graphene, *ACS Nano*, **9**, 11509, 2015.
- [26] S. E. Shafranjuk, Graphene thermal flux transistor, *Nanoscale*, **8**, 19314, 2016.
- [27] P. Dollfus, V. H. Nguyen, and J. Saint-Martin, Thermoelectric effects in graphene nanostructures, *J. Phys. Condens. Matter*, **27**, 133204, 2015
- [28] K. Chen, X. Wang, D. Mo, and S. Lyu. Thermoelectric Properties of Transition Metal Dichalcogenides: From Monolayers to Nanotubes, *J. Phys. Chem. C*, **119**, 26706, 2015
- [29] D. Lembke, S. Bertolazzi, and A. Kis, Single-Layer MoS₂ Electronics, *Acc. Chem. Res*, **48**, 100, 2015.
- [30] D. Lembke and A. Kis, Breakdown of High-Performance Monolayer MoS₂ Transistors, *ACS Nano*, **6**, 10070, 2012.
- [31] B. Radisavljevic, M. B. Whitwick, and A. Kis, Integrated Circuits and Logic Operations Based on Single-Layer MoS₂, *ACS Nano*, **5**, 9934, 2011.
- [32] B. Radisavljevic, A. Radenovic, J. Brivio, V. Giacometti, and A. Kis, Single-layer MoS₂ transistors, *Nat. Nanotechnol*, **6**, 147, 2011.
- [33] K. F. Mak, C. Lee, J. Hone, J. Shan, and T. F. Heinz, Atomically Thin MoS₂: A New Direct-Gap Semiconductor, *Phys. Rev. Lett*, **105**, 136805, 2010.
- [34] J. Pu, Y. Yomogida, K. K. Liu, L. J. Li, Y. Iwasa, and T. Takenobu, Highly Flexible MoS₂ Thin-Film Transistors with Ion Gel Dielectrics, *Nano Lett*, **12**, 4013, 2012.
- [35] S. Bertolazzi, J. Brivio, and A. Kis, Stretching and Breaking of Ultrathin MoS₂, *ACS Nano*, **5**, 9703, 2011.
- [36] K. K. Kam, B. A. Parkinson, Detailed photocurrent spectroscopy of the semiconducting group VIB transition metal dichalcogenides, *J. Phys. Chem.* **86**, 463, 1982.
- [37] J. A. Wilson, A. D. Yoffe, The transition metal dichalcogenides discussion and interpretation of the observed optical, electrical and structural properties, *Advances in Physics*, **18**, 73, 1969.

- [38] A. N. Enyashin and G. Seifert, Electronic Properties of MoS₂ Monolayer and Related Structures. *Nanosystems: Physics, Chemistry, Mathematics*, **5**, P. 517, 2014.
- [39] K. S. Novoselov, D. Jiang, F. Schedin, T. J. Booth, V. V. Khotkevich, S. V. Morozov, A. K. Geim, Two-dimensional atomic crystals, *Proc. Natl. Acad. Sci. U S A*, **102**, 30, 2005.
- [40] M. Buscema, M. Barkelid, V. Zwiller, H. S. J. van der Zant, G. A. Steele, and A. Castellanos-Gomez, Large and Tunable Photo Thermoelectric Effect in Single-Layer MoS₂, *Nano Lett*, **13**, 358, 2013.
- [41] Jing Wu, H. Schmidt, K. Kumar A., X. Xu, G. Eda, B. Özyilmaz, Large Thermoelectricity via Variable Range Hopping in Chemical Vapor Deposition Grown Single-layer MoS₂, *Nano Lett*, **14**, 2730, 2014.
- [42] K. Kaasbjerg, K. S. Thygesen, and K. W. Jacobsen, Phonon-limited mobility in n-type single-layer MoS₂ from first principles, *Phys. Rev. B*, **85**, 115317, 2012
- [43] A. Korm'anyos, V. Zolyomi, N. D. Drummond, P. Rakytá, G. Burkard, and V. I. Fal'ko, Monolayer MoS₂: trigonal warping, the valley, and spin-orbit coupling effects, *Phys. Rev. B*, **88**, 045416, 2013.
- [44] Y. M. Zuev, W. Chang, and P. Kim, Thermoelectric and Magnetothermoelectric Transport Measurements of Graphene, *Phys. Rev. Lett*, **102**, 096807, 2009.
- [45] J. P. Fleurial, L. Gamliard, R. Triaouler, H. Scherrer, and S. Scherrer, Thermal properties of high quality single crystals of bismuth telluride—Part I: Experimental characterization, *J. Phys. Chem. Solids*, **49**, 1237, 1988.
- [46] A. L. Bassi, A. Bailini, C. S. Casari, F. Donati, A. Mantegazza, M. Passoni, V. Russo, and C. E. Bottani, Thermoelectric properties of Bi–Te films with controlled structure and morphology, *Appl. Phys*, **105**, 124307, 2009.
- [47] J. P. Small, K. M. Perez, and P. Kim, Modulation of TE Power of Individual Carbon Nanotubes, *Phys. Rev. Lett*, **91**, 256801, 2003.
- [48] J. Moon, J. H. Kim, Z. C.Y. Chen, J. Xiang, and R. Chen, Gate-Modulated Thermoelectric Power Factor of Hole Gas in Ge–Si Core–Shell Nanowires, *Nano Lett*.

- 13**, 1196, 2013.
- [49] P. Wu, J. Gooth, X. Zianni, S. F. Svensson, J. G. Gluschke, K. A. Dick, C. Thelander, K. Nielsch, and H. Linke, Large Thermoelectric Power Factor Enhancement Observed in InAs Nanowires, *Nano Lett*, **13**, 4080–4086, 2013.
- [50] M. Kayyalha, J. Maassen, M. Lundstrom, L. Shi, and Y. P. Chen, Gate-tunable and thickness-dependent electronic and thermoelectric transport in few-layer MoS₂, *J. Appl. Phys*, **120**, 134305, 2016.
- [51] K. Hippalgaonkar, Y. Wang, Y. Ye, D. Y. Qiu, H. Zhu, Y. Wang, J. Moore, S. G. Louie, and X. Zhang, High thermoelectric power factor in two-dimensional crystals of MoS₂, *Phys. Rev. B*, **95**, 115407, 2017.
- [52] J. Suh, T. E. Park, D. Y. Lin, D. Fu, J. Park, H. J. Jung, Y. Chen, C. Ko, C. Jang, Y. Sun, R. Sinclair, J. Chang, S. Tongay, and J. Wu, Doping against the Native Propensity of MoS₂: Degenerate Hole Doping by Cation Substitution, *Nano Lett*, **14**, 6976, 2014.
- [53] G. Mirabelli, M. Schmidt, B. Sheehan, K. Cherkaoui, S. Monaghan, I. Povey, M. McCarthy, A. P. Bell, R. Nagle, F. Crupi, P. K. Hurley, and R. Duffy, Back-gated Nb-doped MoS₂ junctionless field-effect-transistors, *AIP Advances*, **6**, 025323, 2016.
- [54] K. Dolui, I. Rungger, C. D. Pemmaraju, S. Sanvito, Possible doping strategies for MoS₂ monolayers: An ab initio study, *Phys. Rev. B*, **88**, 075420, 2013.
- [55] M. R. Laskar, D. N. Nath, L. Ma, E. W. Lee, C. H. Lee, T. Kent, Z. Yang, R. Mishra, M. A. Roldan, J. C. Idrobo, S. T. Pantelides, S. J. Pennycook, R. C. Myers, Y. Wu, and S. Rajan, p-type doping of MoS₂ thin films using Nb, *Appl. Phys. Lett*, **104**, 092104, 2014.
- [56] H. Schäfer, *Chemical Transport Reactions* (Academic Press, New York, 1964).
- [57] M. Binnewies, R. Glaum, M. Schmidt, and P. Schmidt, Chemical Vapor Transport Reactions – A Historical Review, *Z. Anorg. Allg. Chem.* **619**, 219, 2013.
- [58] B. Radisavljevic, A. Radenovic, J. Brivio, V. Giacometti, and A. Kis, Single-layer MoS₂ transistors, *Nature Nanotech*, **6**, 147-150, 2011.
- [59] R. Nitsche, H. U. Bölsterli, M. Lichtensteiger, Crystal growth by chemical transport

- reactions—I: Binary, ternary, and mixed-crystal chalcogenides, *J. Phys. Chem. Solids*, **21**, 199, 1961.
- [60] Keiji Ueno, Introduction to the Growth of Bulk Single Crystals of Two-Dimensional Transition-Metal Dichalcogenides, *J. Phys. Soc. Jpn.* **84**, 121015, 2015.
- [61] Makoto Mikamia, Toshiaki Eto, JiFeng Wang, Yoshihiko Masa, Minoru Isshiki, Growth of zinc oxide by chemical vapor transport, *Journal of Crystal Growth*, **276**, 389, 2005.
- [62] MoS₂, Powder Diffr., **1**, 265, 1986.
- [63] J. A. Wilson, A. D. Yoffe, The transition metal dichalcogenides discussion and interpretation of the observed optical, electrical and structural properties, *Adv. Phys.* **18**, 193, 1969.
- [64] Viktoriya V. Ivanovskaya, Alberto Zobelli, Alexandre Gloter, Nathalie Brun, Virginie Serin, Christian Colliex, *Ab initio* study of bilateral doping within the MoS₂-NbS₂ system, *Phys. Rev. B*, **78**, 134104, 2008.
- [65] A. Allain, J. Kang, K. Banerjee, and A. Kis, Electrical contacts to two-dimensional semiconductors, *Nature Materials*, **14**, 1195, 2015.
- [66] C. Gong, L. Colombo, R. M. Wallace, and K. Cho, The Unusual Mechanism of Partial Fermi Level Pinning at Metal–MoS₂ Interfaces, *Nano Lett*, **14**, 1714, 2014.
- [67] S. McDonnell, C. Smyth, C. L. Hinkle, and R. M. Wallace, MoS₂–Titanium Contact Interface Reactions, *ACS Appl. Mater. Interfaces*, **8**, 8289, 2016.
- [68] A. Neal, H. Liu, J. Gu, and P. Ye, Metal Contacts to MoS₂: A Two-Dimensional Semiconductor. In 70th Annual Device Research Conference (DRC), June 18–20, *IEEE*: University Park, PA, pp 65–66, 2012.
- [69] J. Sun, W. Wang, M. Muruganathan, and H. Mizuta, Low pull-in voltage graphene electromechanical switch fabricated with a polymer sacrificial spacer, *Appl. Phys. Lett*, **105**, 033103, 2014.
- [70] H. Nagata, T. Shinriki, K. Shima, M. Tamai, and E. M. Haga, Improvement of bonding

- strength between Au/Ti and SiO₂ films by Si layer insertion, *J. Vac. Sci. Technol. A*, **17**, 1018, 1999.
- [71] K. Nagashio, T. Nishimura, K. Kita, and A. Toriumi, Contact resistivity and current flow path at metal/graphene contact, *Appl. Phys. Lett.*, **97**, 143514, 2010.
- [72] Physical Property Measurement System Thermal Transport Option User's Manual
- [73] H. Wang, Y. Pei, A. D. LaLonde, and G. J. Snyder, Weak electron–phonon coupling contributing to high thermoelectric performance in n-type PbSe, *PNAS*, **109**, 9705, 2012.
- [74] G. Kogo, A. K. Pradhan, and U. N. Roy, Thermoelectric Behavior of PbSe Single, *ECS Journal of Solid State Science and Technology*, **6**, N3006, 2017.
- [75] H. Ikedaa and F. Salleh, Influence of heavy doping on Seebeck coefficient in silicon-on-insulator, *Appl. Phys. Lett.* **96**, 012106, 2010.
- [76] S. Das, H. Chen, A. V. Penumatcha, and J. Appenzeller, High Performance Multilayer MoS₂ Transistors with Scandium Contacts, *Nano Lett.*, **13**, 100, 2013.
- [77] R. Kato and I. Hatta, Thermal Conductivity Measurement of Thermally-Oxidized SiO₂ Films on a Silicon Wafer Using a Thermo-Reflectance Technique, *International Journal of Thermophysics*, **26**, 179, 2005.
- [78] N. F. Mott and E. A. Davis, *Electronic Processes in Non-Crystalline Materials*. Clarendon Press, Oxford, 1979, p. 34.
- [79] E. Conwell and V. F. Weisskopp, Theory of Impurity Scattering in Semiconductors, *Phys. Rev.* **77**, 388, 1950.
- [80] P. W. Anderson, E. Abrahams, and T. V. Ramakrishnan, Possible Explanation of Nonlinear Conductivity in Thin-Film Metal Wires, *Phys. Rev. Lett.* **43**, 718, 1979.
- [81] G. Bergmann, Physical interpretation of weak localization: A time-of-flight experiment with conduction electrons, *Phys. Rev. B*, **28**, 2914, 1983.
- [82] G. Bergmann, Weak localization in thin films: a time-of-flight experiment with conduction electrons, *Phys. Rep.* **107**, 1, 1984.

- [83] J. Han, S. Wang, D. Qian, F. Song, X. Wang, X. Wang, B. Wang, M. Han, J. Zhou, Room-temperature observations of the weak localization in low-mobility graphene films, *J. Appl. Phys.* **114**, 214502, 2013.
- [84] S. Nakaharai, T. Iijima, S. Ogawa, S. Suzuki, S.-L. Li, K. Tsukagoshi, S. Sato, N. Yokoyama, Conduction Tuning of Graphene Based on Defect-Induced Localization, *ACS Nano*, **7**, 5694, 2013.
- [85] D. M. Rowe, *Materials, Preparation, and Characterization in Thermoelectrics*. CRC Press, Taylor & Francis Group, 2012, Ch. 7.
- [86] O. Eibl, K. Nielsch, N. Peranio, F. Völklein, *Thermoelectric Bi_2Te_3 Nanomaterials*. Wiley-VHC Verlag, GmbH&Co. KGaA, 2012, Ch. 5.
- [87] T. J. Wieting, M. Schlüter, *Physics and Chemistry of Materials with layered structures* Volume 3, D. Reidel Publishing Company, 1979, p. 447.
- [88] B. R. Nag, *Electron Transport in Compound Semiconductors*. Springer-Verlag Berlin Heidelberg New York, 1980, p. 174.
- [89] P. Hohenberg and W. Kohn, Photoemission Studies of Copper and Silver: Theory, *Phys. Rev.* **136**, 5188, 1964.
- [90] W. Kohn and L. J. Sham, Self-Consistent Equations Including Exchange and Correlation Effects, *Phys. Rev.* **140**, 1133, 1965.
- [91] J. P. Perdew and Y. Wang, Accurate and simple analytic representation of the electron-gas correlation energy, *Phys. Rev. B*, **45**, 13244, 1992.
- [92] J. P. Perdew, K. Burke, and M. Ernzerhof, Generalized Gradient Approximation Made Simple, *Phys. Rev. Lett.*, **77**, 3865, 1996.
- [93] B. Delley, From molecules to solids with the DMol3 approach, *J. Chem. Phys.* **113**, 7756, 2000.
- [94] A. Kumar and P. K. Ahluwalia, A First Principle Comparative Study of Electronic and Optical Properties of 1H-MoS₂ and 2H-MoS₂, *Materials Chemistry and Physics*, **135**, 755, 2012.

- [95] C. Ataca and S. Ciraci, Functionalization of Single-Layer MoS₂ Honeycomb Structures *Journal of Physical Chemistry C*, **115**, 13303, 2011.
- [96] S. Sahoo, A. P.S. Gaur, M. Ahmadi, M. J-F Guinel, and R. S. Katiyar, Temperature Dependent Raman Studies and Thermal Conductivity of Few Layer MoS₂, *J. Phys. Chem. C*, **117**, 9042, 2013.

Acknowledgements

First of all, I would like to express my gratitude to all those who supported me to complete this dissertation. Especially, I am deeply indebted to my supervisor, Prof. Mikio Koyano, who has patiently provided useful knowledge in many fields, many valuable facilities, great encouragement, and advice for me to proceed through the doctoral program at JAIST. He has been inspired me to become a better and better person.

I would like to express my deep and sincere gratitude to Prof. Hiroshi Mizuta and Prof. Yuzuru Takamura for kindly support of many wonderful facilities. Their generous support has had a remarkable influence on my motivation and progress in research.

I would like to thank Associate Prof. Masashi Akabori. He provided me with helpful discussion, assistance with the experimental operation and great experience to do the experiment.

I also would like to thank Prof. Junichiro Shiomi and Asso. Prof. Dam Hieu Chi for reading and giving me useful comments on my thesis.

I am grateful to many experts for stimulating discussions, especially Dr. Pham Tien Lam and Mr. S. Sueoka, who have taught me and kindly support related to simulation.

I am indebted to Assistant Prof. Masanobu Miyata, Assistant Prof. Manoharan Muruganathan, Assistant Prof. Phan Trong Tue, Dr. Huynh Van Ngoc, Dr. Shunsuke Nishino, Mr. Tasuku Sakuma, Dr. Marek Schmidt, and Mr. Nguyen Thanh Tung for kind support and guidance to do the experiment. Their help has been of great value in my doctoral study.

I would like to express my appreciation to my fellow lab mates for the interesting research discussions, for having fun when working together.

I especially want to thank JAIST and Ministry of Education and Training of Vietnam for financial support and research life during my doctoral course.

I am thankful to the Vietnamese community at JAIST and my dear friends for their supports and encouragements. Finally, I owe my loving thanks to my family for encouraging and supporting me spiritually throughout my life.

List of Figures

Figure 1.1 Energy Statistics and potential TE Generators [2].	1
Figure 1.2 Automotive Climate Control Seat developed by Gentherm [6].	2
Figure 1.3 Good TE materials are typically heavily doped semiconductors (carrier concentration between 10^{19} and 10^{21} carriers per cm^3) [9].	3
Figure 1.4 The Seebeck effect and Peltier effect: (a) The German physicist, T. J. Seebeck, (b) power generation produced by applying a temperature difference to make charge carriers to diffuse from the hot end to the cold end, (c) power generation efficiency in relation to ZT_{ave} ; (d) the French physicist, J. C. A. Peltier, (e) active refrigeration produced by absorbing heat at the lower junction and releasing heat at the higher junction when applying a current through the circuit, (f) cooling efficiency in relation to ZT_{ave} . High ZT_{ave} corresponds to high TE power generation and cooling efficiency [11].	4
Figure 1.5 Electronic DOS for (a) 3D crystalline semiconductor, (b) 2D quantum well, (c) 1D nanowire or nanotube, and (d) 0D quantum dot [23].	7
Figure 1.6 Supercell and crystal structure of bulk MoS_2	7
Figure 1.7 Large Seebeck coefficient of single layer MoS_2 as a function of back gate voltage at different temperatures [41].	8
Figure 1.8 Power factor of thin layer MoS_2 as a function of the V_G [50].	9
Figure 2.1 Quartz ampoules used for the CVT growth of single crystals.	13
Figure 2.2 Powders were introduced into ampoule following the order: I2, S, Mo, Nb.....	14
Figure 2.3 Narrow-necked part of ampoule.	14
Figure 2.4 Uniform mixture inside the evacuated ampoule.	15
Figure 2.5 Temperature distribution inside the furnace tube.	15
Figure 2.6 The period for synthesis of single crystals.	16
Figure 2.7 Single crystals of grown materials by CVT method.	17

Figure 2.8 Big flakes of (a) MoS ₂ and (b) Mo _{0.97} Nb _{0.03} S ₂ .	18
Figure 2.9 The XRD pattern and obtained Miller indices of MoS ₂ , Mo _{0.99} Nb _{0.01} S ₂ , Mo _{0.98} Nb _{0.02} S ₂ , Mo _{0.97} Nb _{0.03} S ₂ and reported MoS ₂ .	18
Figure 2.10 (a) Ultrathin layers are isolated by mechanical exfoliation and	20
Figure 2.11 AFM measurement of thickness of ultrathin layer of Mo _{0.97} Nb _{0.03} S ₂ .	20
Figure 3.1 Schematic structure of the device for measurement of ρ and S .	23
Figure 3.2 Schematic and experimental images for EBL and development.	24
Figure 3.3 Schematic and experimental images for deposition and lift-off. (a) Ti/Au deposited on the exposed area. (b) SEM for observation the deposited metals. (c) Experimental markers after lift-off.	26
Figure 3.4 Schematic and experimental images for etching by using BHF. (a) Exposed area after development. (b) Exposed area after etching. (c) Experimental area after etching.	26
Figure 3.5 Optical images of (a) drawn patterns after development and	27
Figure 3.6 Leakage current in sample # 1.	28
Figure 3.7 IV characteristics between electrodes 5 and 6 for the samples # 1 and # 2.	28
Figure 3.8 The Apollo System for transferring ultrathin layer onto electrodes.	29
Figure 3.9 The schematic diagram for isolating the ultrathin layers.	30
Figure 3.10 Optical images of (a) sample # 1 (b) sample # 2.	30
Figure 3.11 Leakage current in sample # 1 when applying a DC current 35 mA in the heater.	30
Figure 3.12 The design of device for S measurement.	32
Figure 3.13 Experimental device for S measurement.	32
Figure 3.14 Optical image of TTO puck.	33
Figure 3.15 The simulated device based on the real device using Flow 3D simulation model.	35
Figure 3.16 The temperature distribution surrounding Au electrodes and the sample.	36
Figure 3.17 The temperature measurement points on the device	36
Figure 3.18 Time-evolution of temperatures between the two significant points.	37

Figure 3.19 The sectional view of the simulated temperature profile.	37
Figure 4.1 Temperature dependence of S of heavily doped n-type Si.	41
Figure 4.2 (a) Two-probe IV characteristics and (b) overlap of IV characteristics between two-probe and four-probe methods of sample # 1.....	42
Figure 4.3 (a) 3D image and (b) measurement of the length and the width of sample # 1 by using AFM.....	42
Figure 4.4 Thickness measurement of sample # 1 by using AFM.	43
Figure 4.5 Temperature dependence of ρ of sample # 1.	43
Figure 4.6. Thickness measurement of sample # 2 by using AFM.....	44
Figure 4.7 SEM image of sample # 2.	44
Figure 4.8 Temperature dependence of ρ of sample # 2.	45
Figure 4.9 The relationship between the Seebeck voltages of sample # 1 and that of the Si substrate at different temperatures.	47
Figure 4.10 Temperature dependence of thermal conductivity of heavy doped n-type Si substrate used.	48
Figure 4.11 Linear relationship between the TE voltage between electrodes 2–3 and the temperature difference measured at electrodes 6–5 at 300 K of sample # 1.....	48
Figure 4.12 Temperature dependence of S of sample # 1	48
Figure 4.13 Relationship between the Seebeck voltages of sample # 2 and that of the Si substrate at different temperatures.	49
Figure 4.14 Temperature dependence of S of sample # 2.	50
Figure 4.15 Gate voltage dependence of channel current of sample # 1 at a bias voltage from 0 to 1V.....	50
Figure 4.16 The temperature dependence of ρ of two thin samples and bulk at 300 K.	51
Figure 4.17 DOS consisting of weak (Anderson) localized- states (shaded region). E_F is Fermi	

level, E_V is mobility edge.	53
Figure 4.18 Temperature dependence of S of two thin samples, and bulk at 300 K.	55
Figure 4.19 DOS for a 6×6 pristine MoS_2 supercell (black line) and a 6×6 MoS_2 supercell in which one Mo atom is replaced by a Nb (red line). The vertical dashed line shows the Fermi level.	56
Figure 4.20 Fermi level pinning at energy of the midgap surface states N_s , where d is the depth of space-charge region and Φ_s is surface potential.	58
Figure 4.21 Temperature dependence of PF of the sample # 1 and sample # 2.	58

List of Tables

Table 2.1 Amount of powder materials for synthesis by using CVT method	14
Table 2.2 The condition for synthesis	16
Table 2.3 Lattice parameter of synthesized single crystals and reported database MoS ₂	19
Table 4.1 Temperature dependence of S of heavily doped Si.....	40
Table 4.2. Temperature dependence of ρ of sample # 1	42
Table 4.3. Temperature dependence of ρ of sample # 2.....	43

List of activities

◆ Publication Article

Pham Xuan Thi, Masanobu Miyata, Huynh Van Ngoc, Pham Tien Lam, Nguyen Thanh Tung, Manahan Muruganathan, Phan Trong Tue, Masashi Akabori, Dam Hieu Chi, Hiroshi Mizuta, Yuzuru Takamura, and Mikio Koyano; Thermoelectric properties and carrier localization in ultrathin-layer of Nb-doped MoS₂, *Phys. Status Solidi B*, 1800125, 2018.

◆ International conference

Mikio Koyano, Wataru Asai, Pham Xuan Thi, and Masanobu Miyata, Contactless temperature measurement of atomic-layered MoS₂ single crystal supported on silicon substrate, The 37th Annual International and 16th European Conference on thermoelectrics (Cane France, 1-5July2018) [Poster 2, P. 74].

◆ Domestic conference

1. Pham Xuan Thi and Mikio Koyano; Growth of single crystal and mechanical exfoliation of ultrathin layer MoS₂, 2015 Thermoelectric Society of Japan (Poster presentation).
2. Pham Xuan Thi, Marek Schmidt, Phan Trong Tue, Masashi Akabori and Mikio Koyano; Fabrication of suspended ultrathin layer of Mo_{0.97}Nb_{0.03}S₂ for measurement of thermal conductivity, 2016 Thermoelectric Society of Japan (Oral presentation) .

◆ Other

ラマン分光法による界面熱抵抗の直接測定 浅井 渉 , Pham Xuan Thi, 竹内 真里美 , 末岡 伸一 , 宮田 全展 , 小矢野 幹夫第 65 回応用物理学会春期学術講演会 (2018 年 3 月 18 日 , 早稲田大学西早稲田キャンパス) [9.4 応用物性・熱電変換, 18p-P3-18].